

# Capillary hysteresis in sloshing dynamics: a weakly nonlinear analysis

Francesco Viola<sup>1</sup>, P.-T. Brun<sup>1,2</sup> and François Gallaire<sup>1</sup> †,

<sup>1</sup>Laboratory of Fluid Mechanics and Instabilities, École Polytechnique Fédérale de Lausanne, Lausanne, CH-1015, Switzerland

<sup>2</sup>Department of Mathematics, Massachusetts Institute of Technology, Cambridge, Massachusetts 02139, USA

(Received ?; revised ?; accepted ?. - To be entered by editorial office)

The sloshing of water waves in a vertical cylindrical tank is an archetypal damped oscillator in fluid mechanics. The wave frequency is traditionally derived in the potential flow limit (Lamb 1932), and the damping rate results from the combined effects of the viscous dissipation at the wall, in the bulk and at the free surface (Case & Parkinson 1957). Still, the classic theoretical prediction accounting for these effects significantly underestimates the damping rate when compared to careful laboratory experiments (Cocciaro *et al.* 1993). Specifically, theory provides a unique value for the damping rate, while experiments reveal that the damping increases as the sloshing amplitude decreases.

Here, we investigate theoretically the effects of capillarity at the contact line on the decay-time of capillary-gravity waves. To this end, we marry a model for the inviscid waves to a nonlinear empiric law for the contact line that incorporates contact angle hysteresis. The resulting system of equations is solved by means of a weakly nonlinear analysis using the method of multiple scales. Capillary effects have a dramatic influence on the calculated damping rate, especially when the sloshing amplitude gets small: this nonlinear interfacial term increases in the limit of zero wave amplitude. In contrast to viscous damping, where the wave motion decays exponentially, the contact angle hysteresis can act as Coulomb solid friction thus yielding the arrest of the contact line in a finite time.

**Key words:**

## 1. Introduction

Casually shaking a glass of water is sufficient to raise a tempest in it. Large amplitude waves develop and exhibit nonlinear behaviors: overturning, breaking and atomization. However, if the initial amplitude of motion is small enough, the resulting sloshing dynamics is regular. In particular, gravity waves are restricted into modes with a discrete set of wavenumbers, owing to the action of the container walls. The confinement actually exacerbates the viscous dissipation in the fluid, which damps the oscillations and eventually brings the interface to rest. In this small amplitude regime, the non-linearities in the governing equations are negligible and the sloshing modes are classically computed in the limit of potential flow (Lamb 1932). The angular eigenfrequency of the first non-axisymmetric longitudinal mode,  $\omega$ , depends on gravity,  $g$ , the fluid's surface tension,  $\sigma$ ,

† Email address for correspondence: francois.gallaire@epfl.ch

its density  $\rho$  and height  $h$ , and the radius  $R$  of the cylindrical container. The resulting dispersion relation is

$$\omega_n^2 = g\lambda_n \left( 1 + \frac{\sigma}{\rho g} \lambda_n^2 \right) \tanh(\lambda_n h), \quad (1.1)$$

where  $\lambda_n$  are the roots of the first derivative of the  $n_{\text{th}}$ -order Bessel function satisfying  $J'_n(R\lambda_n) = 0$ . Over the course of their motion, those capillary-gravity waves are damped by viscous dissipation occurring (i) at the oscillating Stokes layers at the walls, (ii) in the fluid bulk and (iii) at the free-surface. The damping rates associated with these three dissipation sources may be evaluated via a perturbative approach in the limit of small kinematic viscosity  $\nu$ . Specifically, Case & Parkinson (1957) showed that dissipation in the Stokes layers – scaling as  $\sqrt{\nu}$  – is stronger than that in the bulk, scaling linearly with  $\nu$ . Last, the dissipation at the free surface is even smaller, scaling as  $\nu^{3/2}$  (Ursell 1952). These three damping rates have different scalings with respect to the physical quantities, but all are independent from the amplitude of oscillation, as they were derived from a linear formulation.

Experiments from Benjamin & Ursell (1954); Case & Parkinson (1957); Keulegan (1959) and Cocciaro *et al.* (1991, 1993) have however revealed that the theoretical values of the damping rates significantly underestimate the damping of gravity waves measured in laboratory-size containers. Specifically, Keulegan (1959) carried out an extensive experimental campaign to study the damping of surface standing waves with several liquids, container size and materials. He found that the damping depends on the material of the container and is in general higher than the one provided by the aforementioned linear theory, which – classically – does not account for capillary effects. Further, Keulegan’s pioneering work revealed a dependence of the damping rate on the wave amplitude. He found that the damping rate for small amplitudes – after several wave cycles – was higher than the one observed at larger amplitude, at the beginning of the experiment. Similar results were then reported by different authors both for wetting and non-wetting conditions (Cocciaro *et al.* 1991, 1993; Jiang *et al.* 2004) and were attributed in part to capillary effects.

In summary, experiments evidence the need for a more complete theoretical framework that includes the dissipation due to capillary effects, that was not accounted for in the work of Case & Parkinson (1957), where the interface is assumed to intersect orthogonally the container’s wall (*free-end edge* boundary conditions). This assumption was proven incorrect as experiments reveal that the contact angle  $\theta$  between the fluid-air interface  $\eta(r, \phi, t)$  and the wall is varying throughout the fluid’s motion (Hocking 1987). Additionally, this angle depends on the wetting properties of the wall at the contact line  $\eta(r = R, \phi, t)$  and its velocity. Subsequently, Miles (1967) and Hocking (1987) assumed the contact line velocity to be proportional to the contact angle variation  $\partial\eta/\partial r \approx \pi/2 - \theta$ , through a slip coefficient  $\alpha$

$$\left. \frac{\partial\eta}{\partial t} \right|_R = \alpha \left. \frac{\partial\eta}{\partial r} \right|_R, \quad (1.2)$$

where  $R$  indicates that the derivative is taken at the wall. Hocking (1987) showed that imposing equation (1.2) as a boundary condition in the inviscid sloshing problem yields a finite damping rate, accounting for the viscous dissipation in the dynamic meniscus region where capillary effects dominate. However, the detailed investigation of Cocciaro *et al.* (1993) on the dynamic properties of the meniscus in partial wetting conditions revealed that the slip coefficient  $\alpha$  in the Hocking law (1.2) is a real function of the contact line displacement. This observation points to a more complex nonlinear relation between contact line velocity and contact angle. In particular, the dynamic contact angle

alternates between two values, one for the advancing contact line and a lower one for the receding contact line (see Figure 4 of their paper, (Cocciaro *et al.* 1993)). Such a behaviour agrees well with the model proposed by Dussan (1979) in the framework of a unidirectional flow over a flat plate at low Reynolds number where a difference between the advancing and receding contact angles is observed when the contact line is pinned (static hysteresis) as well as when it slides with a certain velocity over the solid substrate (dynamic hysteresis). This particular contact line model is sketched in Figure (1)(a), where the capillary number is defined as  $Ca = \mu\sqrt{Rg}/\sigma$ . The size of the static hysteresis range depends on the roughness and chemical contamination of the solid surface, see de Gennes (1985) and Leger & Joanny (1992), and varies from few degrees to more than hundred degrees. On the other hand, the dynamic component of the hysteresis is caused by the liquid's inability to flow over the solid surface (Eral *et al.* 2013) and is typically investigated in the lubrication equation framework, which provides a theoretical relation between the dynamic contact angle and contact line velocity, see Voinov (1976) and Cox (1986). This relation is sometime approximated by a linear law as in the case of sliding droplets of silicone oil (Rio *et al.* 2005; Le Grand *et al.* 2005) or of water (Puthenveetil *et al.* 2013), where the slip coefficient is seen to be in the order of  $\alpha = 50$  rad and  $\alpha = 100$  rad for advancing and receding contact line, respectively.

Furthermore, Cocciaro *et al.* (1993) showed that depending on the maximum displacement of the free surface, two different regimes of nonlinear damping were found: a higher and a smaller amplitude regime. In the first one, the contact line *slides* on the solid walls and the damping coefficient greatly increases when the amplitude of oscillation decreases until it reaches a maximum value. Then, this coefficient decreases. The interface pins and the small amplitude regime is reached. The contact line remains at the same locus (*pinned-end edge* condition) and the macroscopic contact angle oscillates around its static value. During this pinned regime the bulk motion was seen to decay with constant damping rate.

The purpose of this work is to investigate theoretically the effect of contact line hysteresis on the pinning of the free-edge mode in partial wetting conditions. This regime corresponds to the high to small amplitude transition observed in Cocciaro *et al.* (1993). We aim to provide a theoretical framework rationalizing the dependence of damping on the amplitude of motion. To this end, we consider inviscid waves subjected to a realistic nonlinear contact line law inspired by the hysteresis law proposed by Dussan (1979), which is described in the next section. The resulting system of equations is solved by means of a weakly nonlinear analysis using the method of multiple scale Stuart (1960). We finally derive a general asymptotic formulation that accounts for nonlinear interfacial effects at the contact line.

The paper is organized as follows. The governing equations, including the contact line model with hysteresis, are presented in § 2. The weakly non linear stability analysis is formulated in § 3, where we compute the fundamental sloshing global mode and derive the governing amplitude equation considering two possible distinguished limits. In § 4, results are discussed, focusing on the dissipative effect of the contact angle hysteresis. Conclusions and perspectives are finally outlined in § 5.

## 2. Governing equations

Let us consider a vertical cylindrical container of radius  $R$  filled to a depth  $H$  with a liquid of density  $\rho$ . A cylindrical coordinate system is defined, where  $z$  is the vertical direction corresponding to the axis of the container, and the zero is set at the unperturbed interface position at the centerline,  $r$  is the radial direction and  $\phi$  is the azimuth (see

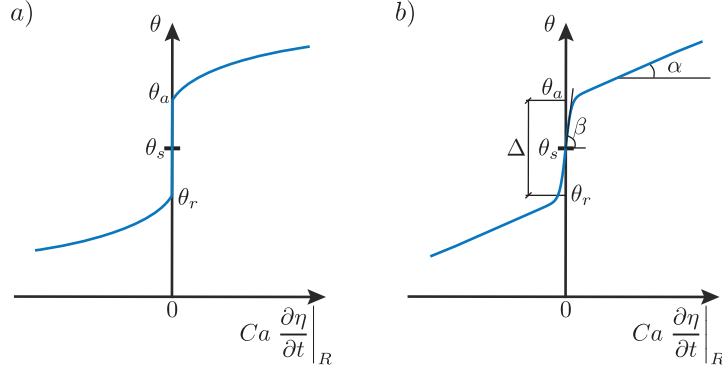


FIGURE 1. Sketch of two contact line models with contact angle,  $\theta$ , as a function of the contact line velocity times the capillary number  $Ca = \mu\sqrt{Rg}/\sigma$ . (a) The nonlinear model of Dussan (1979) with static hysteresis range  $[\theta_r, \theta_a]$  is shown. (b) The nonlinear contact line model (2.5) used in this work is shown. It corresponds to the linear Hocking law (1.2) with slip coefficient  $\alpha$ , augmented with a steep dynamic hysteresis range of size  $\Delta$ .

Figure 2). The fluid motion associated to a displacement of the interface,  $\eta$ , is irrotational outside the viscous boundary layers at the walls and at the interface. In the inviscid limit, the fluid velocity is derived from a velocity potential  $\Phi$ , which satisfies the continuity equation

$$\Delta\Phi = 0, \quad (2.1)$$

together with symmetry condition on the axis ( $\Phi|_{r=0} = 0$ ) and the no penetration condition at the walls:

$$\frac{\partial\Phi}{\partial r}\Big|_{r=1} = 0, \quad \frac{\partial\Phi}{\partial z}\Big|_{z=-H/R} = 0. \quad (2.2)$$

In the following, quantities are made nondimensional by the radius,  $R$ , and the characteristic velocity  $\sqrt{gR}$ . At  $z = \eta$ , the kinematic boundary condition is such that no flow is allowed through the interface:

$$\frac{\partial\eta}{\partial t} = -\frac{\partial\Phi}{\partial r}\frac{\partial\eta}{\partial r} - \frac{1}{r^2}\frac{\partial\Phi}{\partial\phi}\frac{\partial\eta}{\partial\phi} + \frac{\partial\Phi}{\partial z} \quad \text{at } z = \eta, \quad (2.3)$$

and Laplace law prescribes the relation between the pressure,  $p$ , and the local curvature,  $\chi(\eta)$ , namely:

$$-p|_{\eta} = \frac{\chi(\eta)}{Bo} \quad \text{at } z = \eta, \quad (2.4)$$

where the Bond number prescribes the relative magnitude of interfacial effects and gravity  $Bo = \rho g R^2 / \sigma$ , where  $\sigma$  is the surface tension.

We turn to define the boundary condition at the contact line  $\eta(r = 1, \phi, t)$ , which plays a central role in our problem. Rather than the classic free-end edge condition  $\partial\eta/\partial r|_{r=1} = 0$  or the Hocking law in eq. (1.2), we adopt a contact line model shown in Figure 1(b). In addition to the linear relation between dynamic contact angle  $\theta$ , and contact line velocity  $\partial\eta/\partial t|_{r=1}$ , we have modified this model to include a contact angle steplike variation of size  $\Delta$  for small velocities:

$$\theta - \theta_s = \alpha Ca \frac{\partial\eta}{\partial t}\Big|_{r=1} + \frac{\Delta}{2} \tanh\left(\beta Ca \frac{\partial\eta}{\partial t}\Big|_{r=1}\right), \quad (2.5)$$

The model (2.5) is depicted in Figure 1(b), where  $\alpha$  is the linear slip coefficient and the steepness parameter  $\beta \gg 1$  sets the velocity scale at which the contact angle undergoes

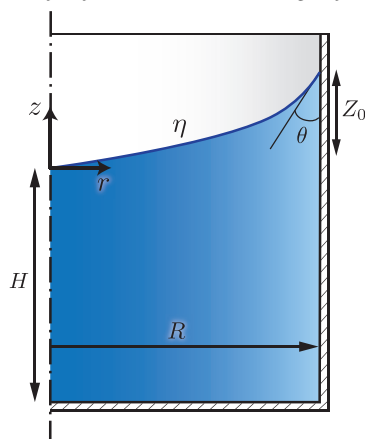


FIGURE 2. Geometry of the circular basin of internal radius  $R$ , which is filled with a liquid column of depth  $H$ . The interface  $\eta$  intersects the vertical wall with the dynamic contact angle  $\theta$ . The amplitude  $Z_0$  denotes the maximum initial interface displacement.

a variation of size  $\Delta$ , referred to as the hysteresis range here after. This rapid variation of the contact angle at small velocities is given by the hyperbolic tangent term in equation (2.5), which is introduced to mimic the static hysteresis range present in Figure 1(a) through a steep dynamic hysteresis. It will become clear to the reader in section 4 that the scaling of these coefficients,  $\alpha$ ,  $\Delta$ ,  $\beta$ , with the amplitude of oscillation will greatly affect the attenuation of the sloshing waves.

Observe that we set the slip coefficient  $\alpha$  constant during the advancing and receding phase, meaning that the contact angle increases when the contact line advances exactly as the opposite as the contact angle decreases when the contact line recedes. Incidentally, we hope that this choice will help highlight the role of  $\Delta$  in the problem. Note that even if the flow is considered inviscid in the domain, viscous forces balance capillary forces at the contact line. As a consequence, eq. (2.5) depends on the capillary number,  $Ca$ . In the following, we use equation (2.5) to model the sloshing of capillary-gravity waves in a cylindrical basin which is imposed as a boundary condition on  $\eta$  at the contact line due to the geometrical relation:

$$\left. \frac{\partial \eta}{\partial r} \right|_{r=1} = \cot(\theta). \quad (2.6)$$

### 3. Weakly nonlinear analysis

The system of equations introduced in the previous section is nonlinear and cannot be solved analytically. We present a weakly nonlinear analysis valid in the limit of small hysteresis range,  $\Delta = \epsilon^2 \hat{\Delta}$  and small values of  $\alpha Ca = \epsilon \hat{\alpha}$ . These physical quantities are scaled in order to generate a distinguished solution which incorporates, as much as possible, all the features of the contact line law (2.5). Furthermore, we consider two possible scalings for the steepness coefficient  $\beta$

$$\beta Ca = \hat{\beta}/\epsilon \text{ (Case I)} \quad \text{or} \quad \beta Ca = \hat{\beta}/\epsilon^2 \text{ (Case II)}, \quad (3.1)$$

that is a large number, in such a way as to induce a rapidly changing contact angle at small contact line velocity, thus approximating a static contact angle hysteresis. Let us

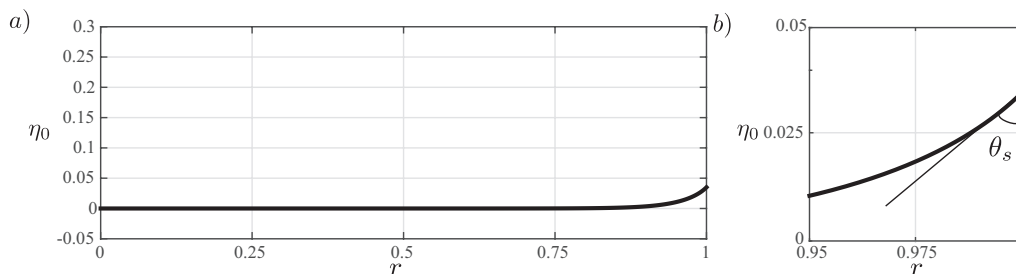


FIGURE 3. In (a) the static meniscus,  $\eta_0$ , is shown as a function of the radial coordinate. In (b) the static contact line region is detailed.

consider the following asymptotic expansion:

$$\begin{aligned}
 \Phi &= \Phi_0 + \epsilon \Phi_1 + \epsilon^2 \Phi_2 + O(\epsilon^3), \\
 \eta &= \eta_0 + \epsilon \eta_1 + \epsilon^2 \eta_2 + O(\epsilon^3), \\
 p &= p_0 + \epsilon p_1 + \epsilon^2 p_2 + O(\epsilon^3), \\
 \theta &= \theta_0 + \epsilon \theta_1 + \epsilon^2 \theta_2 + O(\epsilon^3).
 \end{aligned} \tag{3.2}$$

Substituting the expansion (3.2) in (2.1), (2.3), (2.4) and (2.5), a series of system of equations are obtained at the various orders in  $\epsilon$ . At order  $\epsilon^0$ , the nonlinear problem associated with the shape of the static meniscus will be obtained. At order  $\epsilon$  we recover the classic linear eigenvalue problem for the sloshing modes. Their frequencies correspond to the eigenvalues of this first order system. At the higher order  $\epsilon^2$ , an amplitude equation is obtained:  $A(T)$  is a slow-time modulation that provides the weakly nonlinear correction to the first order solution accounting for our the contact line model. Moreover, in the spirit of multiple scales technique, a *slow* time scale is introduced which is related to the physical *fast* time scale according to:  $T = \epsilon t$ .

### 3.1. Order $\epsilon^0$

At order  $\epsilon^0$ , the static base-state is retrieved. The potential  $\Phi_0$  is null everywhere in the domain and the pressure is hydrostatic,  $p = -z$  in our non-dimensional scheme. The dynamic boundary condition (2.4) reduces to the equation for the static meniscus in radial coordinates, which prescribes the zero-order interface deformation due to capillary effects:

$$-\eta_0 = -\frac{1}{Bo} \chi(\eta_0), \tag{3.3}$$

where  $\chi(\eta_0) = (\eta_{0,rr} + \eta_{0,r}(1 + \eta_{0,r}^2)/r)(1 + \eta_{0,r}^2)^{-3/2}$  is the curvature of  $\eta_0$ , which does not depend on the azimuth. The second-order equation (3.3) is completed with two boundary conditions. At the centerline, the static meniscus regularity condition

$$\left. \frac{\partial \eta_0}{\partial r} \right|_{r=0} = 0 \tag{3.4}$$

holds owing to axisymmetry. The contact line model (2.5), prescribes the boundary condition at  $\eta_0(r = 1)$ :

$$\theta_0 = \theta_s, \tag{3.5}$$

which sets:

$$\left. \frac{\partial \eta_0}{\partial r} \right|_{r=1} = \cot(\theta_s), \tag{3.6}$$

with  $\theta_s \neq 0, 180^\circ$  according to partial wetting conditions at the liquid meniscus. Equation (3.3) is nonlinear in  $\eta_0$  and is solved using an iterative Newton method, see Appendix A.1 for details on the numerical method.

Figure 3(a) shows the static meniscus  $\eta_0(r)$  in the case of  $\theta_s = \pi/4$  and  $Bo = 500$ , which typically corresponds to the value one would obtain for  $g = 9.81 \text{ m/s}^2$  with a glass (here  $R = 0.05 \text{ m}$ ) filled with water ( $\rho = 10^3 \text{ kg/m}^3$ ,  $\mu = 10^{-3} \text{ kg/(ms)}$ ,  $\sigma = 70 \text{ mN/m}$ ). The interface does not depend on  $H$  and is basically flat in the domain aside from a region close to the wall spanning over at a distance of the order of the capillary length,  $\sqrt{\sigma/\rho g} \approx 0.05 R$  here. In Fig. 3(b) equal axis are used to show that  $\eta_0$  intersect the wall with the prescribed static contact angle  $\theta_s = \pi/4$ . We now turn to the next order.

### 3.2. Order $\epsilon$

At order  $\epsilon$  the potential,  $\Phi_1$ , satisfies the first order continuity equation:

$$\Delta \Phi_1 = 0, \quad (3.7)$$

with symmetry condition on the axis and no penetration condition at the vertical and bottom walls. From the unsteady Bernoulli equation, the first order dynamic condition (2.4) flattened at  $\eta_0$  is given by:

$$\frac{\partial \Phi_1}{\partial t} + \eta_1 - \frac{1}{Bo} \frac{\partial \chi(\eta)}{\partial \eta} \Big|_{\eta_0} \eta_1 = 0 \quad \text{at } z = \eta_0, \quad (3.8)$$

where the last term is the first-order variation of the curvature  $\chi(\eta)$  associated with a small perturbation  $\epsilon \eta_1$  :

$$\frac{d\chi(\eta)}{d\eta} \Big|_{\eta_0} \eta_1 = \underbrace{\frac{(1 + \eta_{0,r}^2) - 3r\eta_{0,r}\eta_{0,rr}}{(1 + \eta_{0,r}^2)^{5/2}}}_{a(r)} \frac{1}{r} \frac{\partial \eta_1}{\partial r} + \underbrace{\frac{1}{(1 + \eta_{0,r}^2)^{3/2}}}_{b(r)} \frac{\partial^2 \eta_1}{\partial r^2} + \underbrace{\frac{1}{(1 + \eta_{0,r}^2)^{1/2}}}_{c(r)} \frac{1}{r^2} \frac{\partial^2 \eta_1}{\partial \phi^2}. \quad (3.9)$$

Then, the first order kinematic boundary condition reads:

$$\frac{\partial \eta_1}{\partial t} = - \frac{\partial \Phi_1}{\partial r} \Big|_{\eta_0} \frac{\partial \eta_0}{\partial r} + \frac{\partial \Phi_1}{\partial z} \Big|_{\eta_0} \quad \text{at } z = \eta_0, \quad (3.10)$$

where the radial and the vertical derivative of the potential  $\Phi_1$  correspond to the radial and vertical velocity at  $z = \eta_0$ . The term  $\partial \eta_0 / \partial r$  is the radial derivative of the zero-order interface obtained at previous order. The contact line condition at  $\epsilon$  is  $\theta_1 = 0$ , which implies:

$$\frac{\partial \eta_1}{\partial r} \Big|_{r=1} = 0, \quad (3.11)$$

and corresponds to the free-edge boundary condition.

By defining the state variable  $\mathbf{q}_1 = (\Phi_1, \eta_1)$ , the system of equations can be written in compact form using equations (3.7) and (3.8) as state equations:

$$(\partial_t \mathcal{B} - \mathcal{A}) \mathbf{q}_1 = \mathbf{0}, \quad (3.12)$$

where the linear operators are defined by:

$$\mathcal{B} = \begin{pmatrix} 0 & 0 \\ I_\eta & 0 \end{pmatrix}, \quad \mathcal{A} = \begin{pmatrix} \Delta & 0 \\ 0 & I - \frac{1}{Bo} \frac{\partial \chi(\eta)}{\partial \eta} \Big|_{\eta_0} \end{pmatrix}. \quad (3.13)$$

Equation (3.12) is subject to the boundary conditions at the interface (3.10) and at the contact line (3.11). In addition, the axisymmetry condition  $\Phi_1 = 0|_{r=0}$  is imposed on

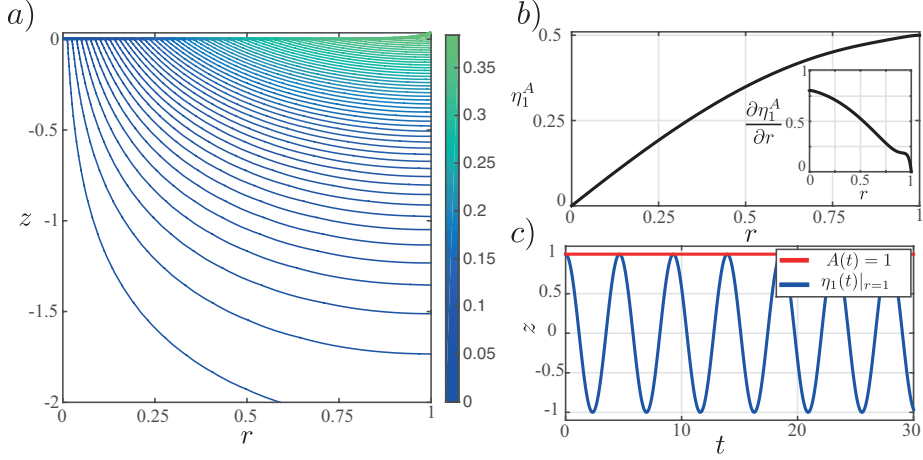


FIGURE 4. First order problem solution for the reference case. (a) Isolines of the potential  $\Phi_1^A$ . In (b) the first order interface  $\eta_1^A$  is shown along with its radial derivative in inset. The first order contact line motion is reported in (c), where the amplitude has been set to one.

the axis, along with the no penetration condition at the solid walls, ( $\frac{\partial \Phi_1}{\partial r}|_{r=1} = 0$  and  $\frac{\partial \Phi_1}{\partial z}|_{z=-H} = 0$ ). The solution of eq. (3.12) then reads:

$$\mathbf{q}_1 = A(T)\mathbf{q}_1^A e^{i\omega t} e^{im\phi} + c.c., \quad (3.14)$$

where *c.c.* stands for the complex conjugate. The amplitude  $A(T)$  is a slow modulation of the flow which depends on the slow time scale  $T = \epsilon t$ , and will be determined at the next order. The integer  $m$  is the azimuthal wavenumber, and the eigenvalue  $i\omega$  is associated with the eigenvector  $\mathbf{q}_1^A$  such that:

$$(i\omega\mathcal{B} - \mathcal{A})\mathbf{q}_1^A = \mathbf{0}, \quad (3.15)$$

with  $\mathbf{q}_1^A = (\Phi_1^A, \eta_1^A)$ . The linear operators  $\mathcal{B}$  and  $\mathcal{A}$  are discretized by mean of Chebyshev collocation method, where a two-dimensional mapping is used to map the computational space to the physical space that has a curved boundary due to the static meniscus  $\eta_0$ . We refer to Appendix A.2 for details on the numerical method and the associated convergence study.

In figure 4(a) the potential  $\Phi_1^A$  is shown for the reference case of  $Bo = 500$ ,  $\theta_s = \pi/4$ ,  $H = 3R$  and  $m = 1$ . We observe that the spatial gradients of  $\Phi_1^A$ , which are connected with the spatial variation of the velocity, are higher at the meniscus region where the domain is curved. In contrast, the potential becomes smooth far from the interface in agreement with classic sloshing theory, which predicts an exponential decay of the wave velocity moving away from the interface. Note that the values reported in the color-bar depends on the normalization of the eigenvector  $\mathbf{q}_1^A$  defined up to a multiplicative factor. Without loss of generality, the eigenvector is normalized here by imposing that  $\eta_1^A(1) = 0.5$ , hence  $\eta_1^A$  a real vector and  $\Phi_1^A$  is a purely imaginary field. In Figure 4(b) the interface  $\eta_1^A$  is shown. According to the boundary conditions at the centerline and at the wall,  $\eta_1^A$  is zero at the centerline and intersects the container walls orthogonally.

Figure 4(c) shows the contact line motion for the case where the slow evolving amplitude  $A(T)$  has been arbitrarily set to one (and will be determined in the next section). Since the flow is inviscid, the contact line keeps oscillating without ever being damped as there is no dissipation mechanism at play yet. The eigenvalue  $\omega$  is thus a real number,

which corresponds to the nondimensional frequency of sloshing. In our reference case we find  $\omega = 1.35$  and the imaginary part is zero to machine precision.

### 3.3. Order $\epsilon^2$

At order  $\epsilon^2$ , the second-order continuity equation reads:

$$\Delta\Phi_2 = 0, \quad (3.16)$$

where  $\Phi_2$  is the second-order velocity potential, which is symmetric with respect to the axis and satisfies the no-penetration condition at the container boundaries. This equation is similar to the first order governing equation (3.7) due to the linearity of the continuity equation (2.1). In contrast, the dynamic condition (2.4) applied to  $\eta_2$  differs from the one at the previous order:

$$\frac{\partial\Phi_2}{\partial t} + \eta_2 - \frac{1}{Bo} \frac{\partial\chi(\eta)}{\partial\eta} \Big|_{\eta_0} \eta_2 = -\frac{\partial\Phi_1}{\partial T} + NRT, \quad (3.17)$$

where forcing terms appear on the right hand side (rhs). According to the definition of  $\mathbf{q}_1 = (\Phi_1, \eta_1)$  in eq. (3.14), the term  $\partial\Phi_1/\partial T$  is the slow time variation of the first order solution which oscillates at system natural frequency determined at the previous order. The terms coming from second-order corrections of both the curvature and the pressure do not resonate. They are quadratic thus not relevant for the further analysis. Consequently, these non resonant terms are not explicitly written in (3.17) but instead are denoted  $NRT$ . We anticipate that, in order to determine the complex amplitude  $A(T)$  at this order, a compatibility condition involving only the resonating terms will be used. Similarly to what was done for the dynamic condition (3.17), we derive the kinematic condition

$$\frac{\partial\eta_2}{\partial t} + \frac{\partial\Phi_2}{\partial r} \Big|_{\eta_0} \eta_{0,r} - \frac{\partial\Phi_2}{\partial z} \Big|_{\eta_0} = -\frac{\partial\eta_1}{\partial T} + NRT, \quad (3.18)$$

where  $\partial\eta_1/\partial T$  is the slow time modulation of the interface motion and  $NRT$  gathers all the non resonating terms.

In compact form, the second order problem is written as:

$$(\partial_t \mathcal{B} - \mathcal{A}) \mathbf{q}_2 = \mathcal{F}_2, \quad (3.19)$$

where  $\mathcal{A}$  is here subjected to the non-homogeneous boundary conditions (3.18) and (3.43). The forcing term on the rhs is:

$$\mathcal{F}_2 = - \begin{pmatrix} 0 \\ \partial\Phi_1/\partial T|_{\eta_0} \end{pmatrix} = - \underbrace{\frac{dA}{dT} \begin{pmatrix} 0 \\ \Phi_1^A|_{\eta_0} \end{pmatrix}}_{\mathcal{F}_2^A} e^{i\omega t} e^{im\phi} + c.c. \quad (3.20)$$

This forcing term can resonate and induce a flow response that diverges as time increases. Hence, a compatibility condition has to be imposed in order to have a non-resonating particular solution to (3.20) of the type  $\mathbf{q}_2 = \hat{\mathbf{q}}_2 e^{i\omega t} e^{im\phi} + c.c.$  and therefore preserve the asymptotic expansion scheme. By substituting this expression in the second order problem (3.19) we get:

$$(i\omega \mathcal{B} - \mathcal{A}) \hat{\mathbf{q}}_2 = \mathcal{F}_2^A. \quad (3.21)$$

This equation has a non-trivial solution if and only if  $\mathcal{F}_2^A$  is orthogonal to the adjoint mode  $\mathbf{q}^\dagger$ , according to Fredholm alternative. The adjoint global mode  $\mathbf{q}^\dagger$  is the solution

of the adjoint equations:

$$(i\omega^\dagger \mathcal{B}^\dagger - \mathcal{A}^\dagger) \mathbf{q}^\dagger = \mathbf{0}, \quad (3.22)$$

where the linear operators  $\mathcal{A}^\dagger$  and  $\mathcal{B}^\dagger$  and the adjoint pulsation  $\omega^\dagger$  are derived by integrating by parts the system of equations (3.12). We refer to Appendix B for the complete derivation of the adjoint equations and the definition of the adjoint mode. The resulting compatibility condition reads:

$$\langle \mathbf{q}^\dagger, (i\omega \mathcal{B} - \mathcal{A}) \hat{\mathbf{q}}_2 \rangle = \langle \mathbf{q}^\dagger, \mathcal{F}_2^A \rangle. \quad (3.23)$$

where the brackets  $\langle \rangle$  define the Hermitian scalar product (B 1). By substituting the expression for  $\mathcal{F}_2^A$  from (3.20), we obtain

$$\langle \mathbf{q}^\dagger, \mathcal{F}_2^A \rangle = -\frac{dA}{dT} \int_{\eta_0} \bar{\eta}^\dagger \Phi_1^A d\eta_0, \quad (3.24)$$

where the symbol  $\int_{\eta_0}$  denotes a surface integral on the zero-order surface  $\eta_0(r)$  with  $d\eta_0 = r dr \sqrt{1 + \eta_{0,r}^2}$ , as detailed in Appendix B. Furthermore, the left hand side of equation (3.23) is non-zero because the kinematic and the contact line conditions are not homogeneous at second order:

$$\langle \mathbf{q}^\dagger, (i\omega \mathcal{B} - \mathcal{A}) \hat{\mathbf{q}}_2 \rangle = \underbrace{\langle (i\omega^\dagger \mathcal{B}^\dagger - \mathcal{A}^\dagger) \mathbf{q}^\dagger, \hat{\mathbf{q}}_2 \rangle}_{=0} + \int_{\eta_0} \bar{\Phi}^\dagger \frac{dA \eta_1^A}{dT} d\eta_0 - \frac{\sin^3 \theta_s}{Bo} \bar{\eta}^\dagger \left. \frac{\partial \hat{\eta}_2}{\partial r} \right|_{r=1}, \quad (3.25)$$

where the integral on the free surface  $\eta_0$  comes from the slow time derivative in the second-order kinematic condition (3.18), and the last term is associated with the contact line model. The detailed calculation yielding these boundary and corner terms are reported in Appendix B.

At this point, the nonlinear contact angle correction due to the contact line model enters in the analysis through the geometrical relation:

$$\left. \frac{\partial \eta_2}{\partial r} \right|_{r=1} = \frac{-\theta_2}{\sin^2(\theta_s)}, \quad (3.26)$$

with

$$\theta_2 + O(\epsilon) = \hat{\alpha} \left. \frac{\partial \eta_1}{\partial t} \right|_{r=1} + \frac{\hat{\Delta}}{2} \tanh \left( \beta Ca \epsilon \left. \frac{\partial \eta_1}{\partial t} \right) \right|_{r=1}, \quad (3.27)$$

where  $\hat{\Delta}$  is the rescaled hysteresis range,  $\Delta = \epsilon^2 \hat{\Delta}$ , and  $\hat{\alpha}$  is the rescaled slip coefficient,  $\alpha Ca = \epsilon \hat{\alpha}$ . In the following we derive the solutions coming from the two possible scalings of the steepness coefficient  $\beta$  introduced in equation (3.1).

#### 3.4. Amplitude equation: Case I, $\beta Ca = \hat{\beta}/\epsilon$

In this case the second order contact line law (3.27) reads

$$\theta_2 = \hat{\alpha} \left. \frac{\partial \eta_1}{\partial t} \right|_{r=1} + \frac{\hat{\Delta}}{2} \tanh \left( \hat{\beta} \left. \frac{\partial \eta_1}{\partial t} \right) \right|_{r=1}, \quad (3.28)$$

In order to impose a compatibility condition in equation (3.25), which is needed to determine the amplitude  $A(T)$  in equation (3.14), the terms oscillating at the natural frequency in the contact line model (3.28) have to be considered, as done for the dynamic

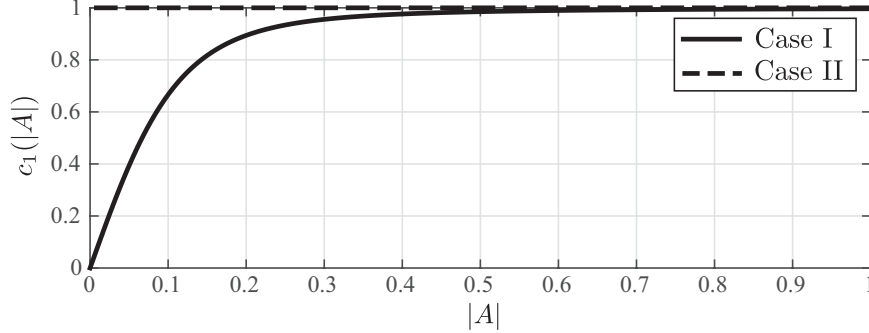


FIGURE 5. First Fourier coefficient  $c_1(|A|)$  of the nonlinear term in the second order contact line model (3.27) shown as a function of the oscillation amplitude  $|A|$  in the case of  $Bo = 500$ ,  $\theta_s = \pi/4$  (so that  $\omega = 1.35$ ) and  $\hat{\beta} = 1$ . The solid line corresponds to case I ( $Ca\beta = \hat{\beta}/\epsilon$ ) whereas case II ( $Ca\beta = \hat{\beta}/\epsilon^2$ ) is shown by dashed line.

and kinematic conditions (3.17) (3.18). However, the  $\tanh$  function is nonlinear and not purely harmonic, but through the Fourier series its  $\omega$ -harmonic may be isolated (see Nayfeh (2008)):

$$\left. \tanh\left(\hat{\beta}\frac{\partial\eta_1}{\partial t}\right)\right|_{r=1} = \tanh\left(\hat{\beta}i\omega A\eta_1^A|_{r=1}e^{i(\omega t+m\phi)} + c.c.\right) = \sum_{k=-\infty}^{\infty} d_k(\phi)e^{ik\omega t} \quad (3.29)$$

The complex amplitude and  $\eta_1^A$  can be decomposed in modulus and phase, namely:  $A(T) = |A(T)|e^{i\vartheta(T)}$  and  $\eta_1^A = |\eta_1^A|e^{i\vartheta_\eta}$ . By defining the variable  $\xi = \omega t + m\phi + \frac{\pi}{2} + \vartheta_\eta|_{r=1} + \vartheta(T)$ , the coefficient  $d_k$  is given by:

$$\begin{aligned} d_k(\phi) &= \frac{\omega}{2\pi} \int_{-\frac{\pi}{\omega}}^{\frac{\pi}{\omega}} \tanh(\hat{\beta}\omega|A||\eta_1^A|_{r=1}|2\cos(\xi))e^{-ik\omega t} dt \\ &= e^{ik(m\phi+\pi/2+\vartheta_\eta+\vartheta(T))} \underbrace{\frac{1}{2\pi} \int_{-\pi}^{\pi} \tanh(\hat{\beta}\omega|A||\eta_1^A|_{r=1}|2\cos(\xi))e^{-ik\xi} d\xi}_{\frac{2}{\pi}c_k(|A|)} \end{aligned} \quad (3.30)$$

where the prefactor  $2/\pi$  has been introduced to simplify the upcoming analysis and the Fourier coefficient  $c_k(|A|)$  is only a function of the amplitude magnitude  $|A|$  since  $\hat{\beta}$  is set by the contact line law and  $\omega$  and  $|\eta_1^A|_{r=1}$  by the first order problem. Consequently, the nonlinear term reads:

$$\left. \tanh\left(\hat{\beta}\frac{\partial\eta_1}{\partial t}\right)\right|_{r=1} = \frac{2}{\pi} \sum_{k=-\infty}^{\infty} c_k(|A|)e^{ik\xi} = \frac{2}{\pi} c_1(|A|)e^{i(\omega t+m\phi+\pi/2+\vartheta_\eta|_{r=1}+\vartheta(T))} + c.c. + NRT, \quad (3.31)$$

where we have isolated the harmonic oscillating at the sloshing natural frequency. The Fourier coefficient  $c_1(|A|)$  can be computed numerically. It varies between the limiting value 1 at large amplitude and 0 when  $|A|$  is small. As anticipated above, the exact shape of the function  $c_1(|A|)$  depends on first order problem and has to be recomputed when the oscillation frequency  $\omega$  or the rescaled steepness coefficient  $\hat{\beta}$  are changed. A typical curve of  $c_1(|A|)$  for the reference case introduced in section 3.2 is shown by solid line in Figure 5. Substituting equation (3.31) in the  $\epsilon$ -order contact line model (3.26) yields:

$$\left. \frac{\partial \eta_2}{\partial r} \right|_{r=1} = -\frac{\hat{\alpha}}{\sin^2(\theta_s)} i\omega \eta_1^A|_{r=1} A e^{i\omega t} e^{im\phi} - \frac{i\hat{\Delta}c_1(|A|)}{\pi \sin^2(\theta_s)} \frac{\eta_1^A|_{r=1}}{|\eta_1^A|_{r=1}} \frac{A}{|A|} e^{i\omega t} e^{im\phi} \Big|_{r=1} + c.c. + NRT, \quad (3.32)$$

where the first term on the rhs is associated to the linear part of the contact line model (2.5) and provides a correction to the dynamic contact angle, found proportional to the contact line velocity. The second term in the rhs is nonlinear with respect to the contact line velocity. Its origin is attributed to the fast dynamic hysteresis, proportional to the rescaled hysteresis range  $\hat{\Delta}$ . Introducing the auxiliary constant  $\kappa$  and the two real damping coefficients  $\zeta$  and  $\chi$ , defined as

$$\kappa = (\bar{\eta}^\dagger \eta_1^A)_{r=1} / \int_{\eta_0} \bar{\eta}^\dagger \Phi_1^A + \bar{\Phi}_1^\dagger \eta_1^A d\eta_0, \quad \zeta = \frac{-i\omega \sin(\theta_s) \hat{\alpha} \kappa}{Bo}, \quad \chi = \frac{-i \sin(\theta_s) \hat{\Delta} \kappa}{\pi Bo |\eta_1^A|_{r=1}}, \quad (3.33)$$

the substitution of expression (3.32) in equation (3.25) yields the compatibility condition

$$\frac{dA}{dT} + \zeta A + \chi c_1(|A|) \frac{A}{|A|} = 0, \quad (3.34)$$

where the last term corresponds to the function  $c_1(|A|)$  multiplying the sign of  $A$ . Since the function  $c_1(|A|)$  is real, decomposing the complex amplitude in modulus and phase,  $A(T) = |A(T)|e^{i\vartheta(T)}$ ,

$$\frac{d\vartheta}{dT} = 0. \quad (3.35)$$

From equation (3.35) we argue that the sloshing frequency is not modified at leading order and that the amplitude phase  $\vartheta(T)$  is set by the initial condition  $\vartheta(T) = \vartheta_0$ . The value of  $|A|$  as a function of time, which dictates the relaxation dynamics caused by the contact line dissipation, can be obtained by numerical integration of (3.34). The corresponding contact line motion that accounts for the weakly non linear correction is:

$$\eta_1|_{r=1} = 2|A(T)| |\eta_1^A|_{r=1} \cos(\omega t + \vartheta_0 + m\phi + \vartheta_\eta|_{r=1}). \quad (3.36)$$

Specifically,  $|A(T)|$  is the nonlinear correction on the amplitude, and  $\vartheta_\eta$  is the phase of  $\eta_1^A|_{r=1}$ , which is nil due to way the eigenmode  $\mathbf{q}_1^A$  has been normalized. It should be noted that  $\eta_1^A$ ,  $\vartheta_\eta$  and  $A(T)$  all depend on the normalization of the direct mode, albeit the final result  $\eta_1$  does not.

We consider, as an illustrative example, the dynamics of the fundamental sloshing mode,  $m = 1$ , following an initial deflection of the interface of amplitude  $Z_0 = \epsilon A_0 = 0.1$  from rest ( $\vartheta_0 = 0$ ) for the set of representative parameters chosen throughout this section. The Bond number and the static contact angle are equal to  $Bo = 500$  and  $\theta_s = \pi/4$ , and the contact line model parameters are set to  $Ca = 0.01$ ,  $\alpha = 60$  rad,  $\Delta = 20^\circ$  and  $\hat{\beta} = 1$ . Figure 6(a) shows the second order contact line motion (blue line) and  $|A(T)|$  (red line). As inferred from (3.35) we find that the sloshing frequency is not modified by capillary effects. The amplitude, contrasts with the first order solution (Figure 4c). The contact line is significantly damped: the wave amplitude is more than hundred times smaller than the initial amplitude of our reference case after forty periods. According to the amplitude equation (3.34) the effective damping appears as the sum of two terms: a linear contribution, weighted by the linear damping coefficient  $\zeta$ , resulting from the linear part of the contact line model and a contribution, scaled by the nonlinear damping coefficient  $\chi$ , originating from the dynamic contact line hysteresis at small velocity. This last contribution is nonlinear in nature. We refer the interested reader to appendix C for a validation of the asymptotic analysis against direct numerical simulation of the governing

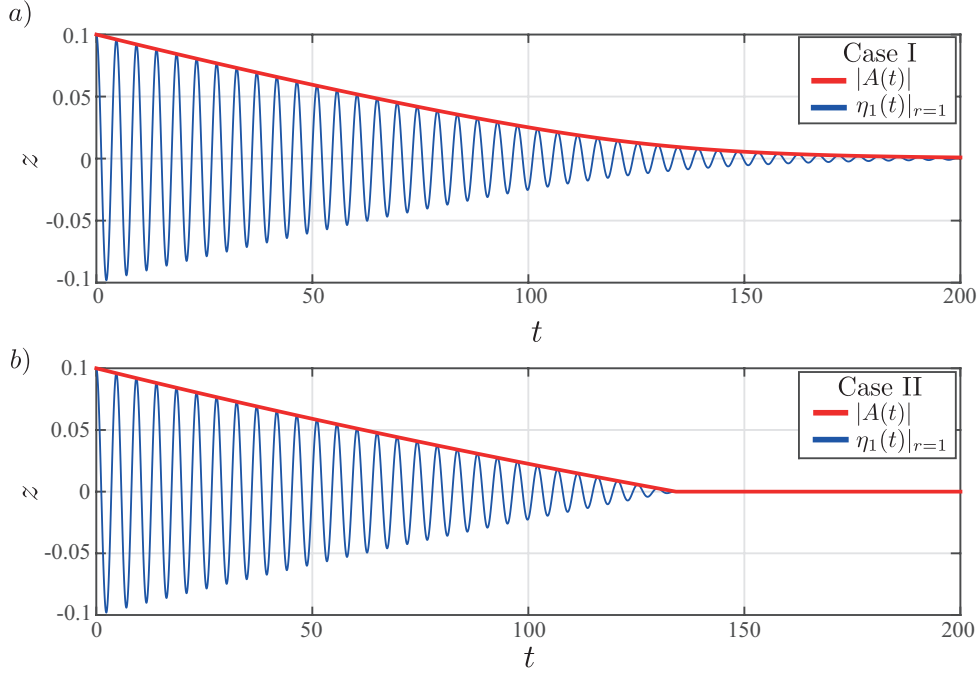


FIGURE 6. Contact line motion (blue line) modulated by the slow time amplitude (red line) of the fundamental free-end edge sloshing mode,  $m = 1$ , following an initial deflection of the interface of amplitude,  $Z_0 = \epsilon A_0 = 0.1$ , from rest ( $\vartheta_0 = 0$ ). The Bond number and the static contact angle are equal to  $Bo = 500$  and  $\theta_s = \pi/4$ , and the contact line model parameters are set to  $Ca = 0.01$ ,  $\alpha = 60$  rad,  $\Delta = 20^\circ$  and  $\hat{\beta} = 6.5$ . The steepness of the contact angle hysteresis is equal to (a) case I ( $Ca\beta = \hat{\beta}/\epsilon$ ) and (b) case II ( $Ca\beta = \hat{\beta}/\epsilon^2$ ).

equations. Let us now consider another distinguished limit of the steepness coefficient  $\beta Ca$  (case II) before deepening the discussion on the capillary damping effects.

### 3.5. Amplitude equation: Case II, $\beta Ca = \hat{\beta}/\epsilon^2$

When the steepness factor  $\beta$  is larger,  $\beta Ca = \hat{\beta}/\epsilon^2$ , the second order contact line law (3.27) reads

$$\theta_2 + O(\epsilon) = \hat{\alpha} \frac{\partial \eta_1}{\partial t} \Big|_{r=1} + \frac{\hat{\Delta}}{2} \tanh \left( \frac{\hat{\beta}}{\epsilon} \frac{\partial \eta_1}{\partial t} \right) \Big|_{r=1}. \quad (3.37)$$

We need to isolate the resonating term in the nonlinear boundary condition in order to impose a compatibility condition in equation (3.25). By taking the Fourier transform of the nonlinear term in equation (3.37) we obtain

$$\tanh \left( \frac{\hat{\beta}}{\epsilon} \frac{\partial \eta_1}{\partial t} \right) \Big|_{r=1} = \tanh \left( \frac{\hat{\beta}}{\epsilon} i\omega A \eta_1^A \Big|_{r=1} e^{i(\omega t + m\phi)} + c.c. \right) = \sum_{k=-\infty}^{\infty} d_k(\phi) e^{ik\omega t} \quad (3.38)$$

The complex amplitude and  $\eta_1^A$  can be decomposed in modulus and phase, namely:  $A(T) = |A(T)|e^{i\vartheta(T)}$  and  $\eta_1^A = |\eta_1^A|e^{i\vartheta_\eta}$ . Using the variable  $\xi = \omega t + m\phi + \frac{\pi}{2} + \vartheta_\eta|_{r=1} + \vartheta(T)$ , the coefficients  $d_k$  are here given by

$$d_k(\phi) = \frac{\omega}{2\pi} \int_{-\frac{\pi}{\omega}}^{\frac{\pi}{\omega}} \tanh(\hat{\beta}/\epsilon\omega|A||\eta_1^A|_{r=1}2\cos(\xi))e^{-ik\omega t} dt. \quad (3.39)$$

The hyperbolic tangent in the integrand can be expanded as the sum of the sign function plus a correction  $f(\epsilon, \xi)$ , which satisfies  $\int_{-\pi}^{\pi} f(\epsilon, \xi) e^{-ik\omega t} d\xi = O(\epsilon)$ . Consequently, equation (3.39) reads:

$$\begin{aligned} d_k(\phi) &= \frac{\omega}{2\pi} \int_{-\frac{\pi}{\omega}}^{\frac{\pi}{\omega}} \operatorname{sgn}(\hat{\beta}/\epsilon\omega|A||\eta_1^A|_{r=1} 2 \cos(\xi)) e^{-ik\omega t} dt + \underbrace{\frac{\omega}{2\pi} \int_{-\frac{\pi}{\omega}}^{\frac{\pi}{\omega}} f(\epsilon, \xi) e^{-ik\omega t} dt}_{O(\epsilon)} \\ &= e^{ik(m\phi + \pi/2 + \vartheta_\eta|_{r=1} + \vartheta(T))} \underbrace{\frac{1}{2\pi} \int_{-\pi}^{\pi} \operatorname{sgn}(\cos(\xi)) e^{-ik\xi} d\xi}_{\frac{2}{\pi} c_k} + O(\epsilon), \end{aligned} \quad (3.40)$$

which further gives

$$\left. \tanh\left(\frac{\hat{\beta}}{\epsilon} \frac{\partial \eta_1}{\partial t}\right)\right|_{r=1} = \frac{2}{\pi} \sum_{k=-\infty}^{\infty} c_k e^{ik\xi} = \frac{2}{\pi} c_1 e^{i(\omega t + m\phi + \pi/2 + \vartheta_\eta|_{r=1} + \vartheta(T))} + c.c. + O(\epsilon) + NRT, \quad (3.41)$$

where we have isolated the harmonic oscillating at the sloshing natural frequency and  $NRT$  groups the non-resonating terms. The Fourier coefficient  $c_1$  does not depend here on the amplitude and is equal to:

$$\frac{2}{\pi} c_1 = \frac{1}{2\pi} \int_{-\pi}^{\pi} \operatorname{sgn}(\cos(\xi)) e^{-i\xi} d\xi = \frac{2}{\pi}, \quad \Rightarrow c_1 = 1. \quad (3.42)$$

Injecting equation (3.41) into the geometrical relation (3.37), and substituting in equation (3.26) one gets

$$\left. \frac{\partial \eta_2}{\partial r}\right|_{r=1} = -\frac{\hat{\alpha}}{\sin^2(\theta_s)} i\omega \eta_1^A|_{r=1} A e^{i\omega t} e^{im\phi} - \frac{i\hat{\Delta}}{\pi \sin^2(\theta_s)} \frac{\eta_1^A|_{r=1}}{|\eta_1^A|_{r=1}} \frac{A}{|A|} e^{i\omega t} e^{im\phi} \Big|_{r=1} + c.c. + NRT. \quad (3.43)$$

As in case I we can distinguish a linear term in the rhs and a nonlinear term attributed to the fast variation of the hysteresis range at small contact line velocity. Specifically, this term only depends on the phase of the velocity, a result consistent with the use of the  $\operatorname{sgn}$  function (that only depends on the sign of its argument). As a result, this term provides a different correction depending whether the interface is advancing or receding.

Substituting (3.43) in equation (3.25) yields the compatibility condition

$$\frac{dA}{dT} + \zeta A + \chi \frac{A}{|A|} = 0, \quad (3.44)$$

where the last term in the lhs corresponds to the sign of  $A$ . Similarly to equation (3.34), the effective damping appears as the sum of a linear contribution, weighted by the linear damping coefficient  $\zeta$ , resulting from the linear part of the contact line model and a nonlinear contribution, scaled by the nonlinear damping coefficient  $\chi$ , originating in the contact line hysteresis.

Decomposing the complex amplitude in modulus and phase,  $A(T) = |A(T)|e^{i\vartheta(T)}$ , equation (3.44) may be integrated analytically:

$$|A(T)| = \left(A_0 + \frac{\chi}{\zeta}\right) e^{-\zeta T} - \frac{\chi}{\zeta}, \quad \vartheta(T) = \vartheta_0, \quad (3.45)$$

where  $A_0$  and  $\vartheta_0$  depend on the initial conditions. Equation (3.45) represents the weakly non linear correction to the first-order solution (3.14) associated with the contact line

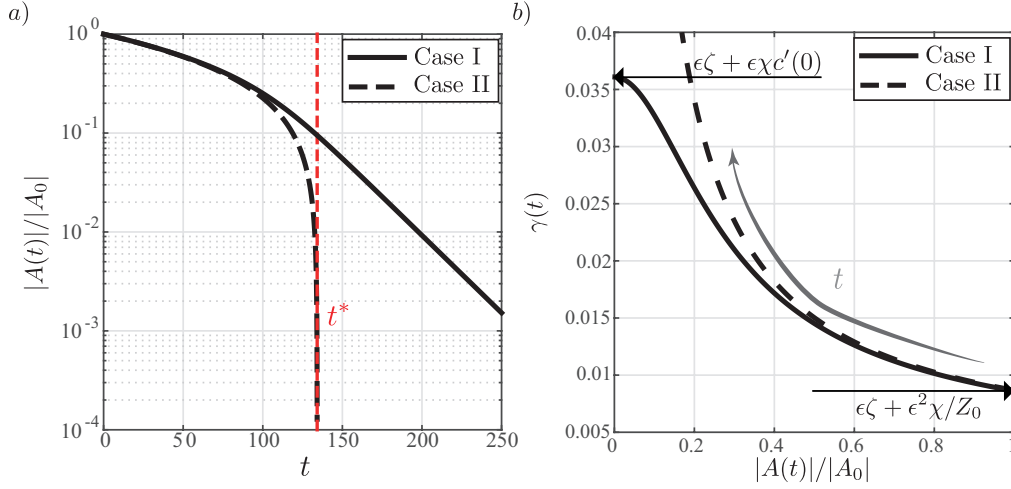


FIGURE 7. a) Amplitude modulation in logarithmic scale versus time and b) capillary damping rate versus the wave amplitude of the fundamental free-end edge sloshing mode,  $m = 1$ , following an initial deflection  $Z_0 = \epsilon A_0 = 0.1$ . The Bond number and the static contact angle are equal to  $Bo = 500$  and  $\theta_s = \pi/4$ , and the contact line model parameters are set to  $Ca = 0.01$ ,  $\alpha = 60$  rad,  $\Delta = 20^\circ$  and  $\hat{\beta} = 6.5$ . The steepness of the dynamic contact angle hysteresis at small contact line velocity is equal to  $Ca\beta = \hat{\beta}/\epsilon$  for case I (solid line) and  $Ca\beta = \hat{\beta}/\epsilon^2$  for case II (black dashed line). The red vertical line depicts the finite time at which the amplitude gets to zero in case I.

model (2.5), yielding the contact line motion (3.36).

The second order contact line motion following an initial deflection of amplitude  $Z_0 = \epsilon A_0 = 0.1$  is shown in Figure 6(b). The same set of parameters used for Figure 6(a) is used, except for the steepness factor  $Ca\beta$ , which is now taken equal to  $1/\epsilon^2$  ( $\hat{\beta} = 1$ ). Similarly to case I, the contact line motion is found to be damped by capillarity. However, the wave attenuation in (b) is faster than the one in (a) where the oscillation still persists for  $t > 200$ . In contrast, in case II, the wave amplitude is seen to decrease abruptly in a linear fashion at the end of the motion (see equation (3.45)), yielding a finite time arrest: the oscillating motion is null for sufficiently large time. These features are discussed in the upcoming section.

#### 4. Discussion

Our multiple scale analysis has revealed the nonlinear nature of sloshing when dynamic capillary hysteresis is included. In this section, we discuss the dynamics of the fundamental sloshing mode, focusing on the wave attenuation:

$$\gamma(t) = -\frac{d \log(|A(et)|/A_0)}{dt} = -\frac{\epsilon}{|A(T)|} \frac{d|A(T)|}{dT}, \quad (4.1)$$

which corresponds to the derivative of the logarithmic decrement shown in Figure 7(a).

##### 4.1. Case I: $\beta Ca = \hat{\beta}/\epsilon$

Substituting the amplitude equation (3.34) in the instantaneous damping rate definition (4.1) we get

$$\gamma(t) = \epsilon\zeta + \epsilon\chi \frac{c_1(|A|)}{|A(et)|}, \quad (4.2)$$

as shown in Figure 7(b) (solid line). The wave attenuation is not constant during sloshing and the instantaneous damping rate depends on the wave amplitude. For sufficiently large amplitude, such that  $c_1(|A|)$  tends to one, the decay is practically exponential with damping rate approaching the limiting value

$$\gamma(t=0) = \epsilon\zeta + \epsilon^2 \frac{\chi}{Z_0}. \quad (4.3)$$

Two contributions to the damping rate thus prevail at initial times: (i) the one associated to the linear contact line friction, which is here proportional to  $\alpha$ , through  $\zeta$ , and (ii) a damping rate proportional to the hysteresis range  $\Delta$ , through  $\chi$ , and inversely proportional to the initial amplitude  $Z_0$ . Note that the second  $1/Z_0$  contribution was found by Miles (1967) in the limit of small critical velocity, and assuming that the mean energy relaxes exponentially. Then the damping rate varies owing to the second term in the right-hand-side of equation (4.2), which has an explicit dependence on  $|A|$ . In particular, the numerator  $c_1(|A|)$  slowly varies for intermediate amplitudes (see Figure 5), whereas the denominator  $|A|$  decreases linearly. Thus, the damping rate increases significantly when the sloshing amplitude decreases. However, at smaller oscillating amplitudes,  $c_1(|A|)$  decreases linearly with respect to  $|A|$ , with slope  $c'(0) = \left. \frac{dc_1}{d|A|} \right|_{|A|=0}$ , and the ratio  $c_1/|A|$  tends to a constant value. As a consequence, the system enters in a low amplitude linear regime, with damping rate

$$\gamma(t=\infty) \rightarrow \epsilon\zeta + \epsilon\chi c'(0) = \epsilon\zeta + \epsilon\chi\pi/2\hat{\beta}\omega|\eta_1^A|_{r=1}, \quad (4.4)$$

and the free-end edge mode decays exponentially.

#### 4.2. Case II: $\beta Ca = \hat{\beta}/\epsilon^2$

In the case of higher hysteresis steepness coefficient, the amplitude equation (3.44) yields

$$\gamma(t) = \epsilon\zeta + \epsilon\chi \frac{1}{|A(\epsilon t)|}, \quad (4.5)$$

which is shown in Figure 7(b) (dashed line). The wave attenuation is seen to depend on the wave amplitude. The decay is roughly exponential at large amplitude, and the damping rate is equal to the one in equation (4.3). The wave attenuation then increases when the amplitude decreases. Rather than reaching a low amplitude linear regime the damping rate keeps increasing. In particular, we find the existence of a finite time  $t^*$  such that the damping rate diverges:

$$\gamma(t=t^*) \rightarrow \infty, \quad (4.6)$$

with,

$$t^* = \frac{1}{\epsilon\zeta} \log \left( 1 + \frac{\zeta Z_0}{\chi \epsilon} \right). \quad (4.7)$$

The finite time singularity of the damping rate yields the arrest of the contact line, whose amplitude becomes exactly zero for  $t = t^*$  (see eq. (3.45)). Recalling that  $\chi \propto \Delta$  (eq. (3.33)), we argue that the contact angle hysteresis at small contact line velocity is at the origin of this finite time arrest of the free-end edge mode. Consistent with this assertion we find that  $t^*$  diverges if  $\Delta$  is set to zero. In this limit the system relaxes exponentially with damping rate  $\epsilon\zeta$ . Conversely, even a small value of the hysteresis range – as small as  $1^\circ$  – is sufficient to induce a significant dissipative effect that, in turn, largely impacts the dynamics, and, in particular, leads to an arrest of free-end edge mode in finite time.

We now turn to investigate the parametric dependence of the time of arrest  $t^*$ . To

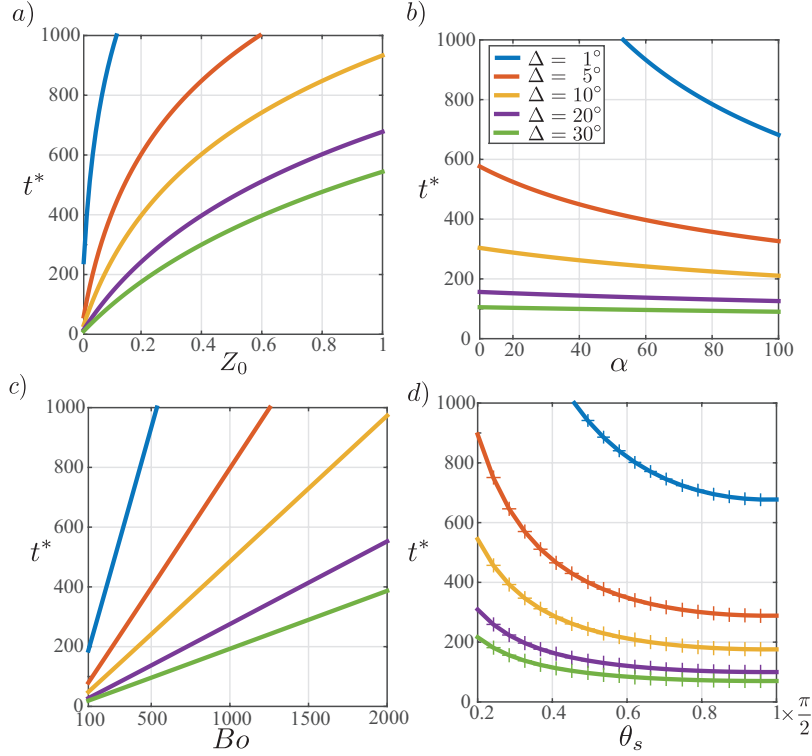


FIGURE 8. Finite time of arrest  $t^*$  reported as a function of a) the initial contact line displacement, b) the slip coefficient, c) the Bond number and d) the static contact angle. The + symbols displayed in (d) correspond to  $t^*$  computed with a finer mesh (see Appendix A), showing convergence with respect to grid resolution.

this end, we use the configuration introduced in section 3 as a reference and vary (i) the Bond number,  $Bo$ , (ii) the static contact angle,  $\theta_s$ , as well as (iii) the contact line model parameters,  $\alpha Ca$  and  $\Delta$ , and (iv) the set of the initial condition,  $Z_0 = \epsilon A_0$ . Using section 3, we anticipate that the first order solution solely depends on  $\theta_s$  and  $Bo$ . The contact line model parameters  $\alpha Ca$  and  $\Delta$ , and the initial condition  $A_0$  only enter the problem at second order. Using the definitions for  $\zeta$  and  $\chi$  introduced in equation (4.7), we obtain a scaling law for  $t^*$ :

$$t^* \propto \frac{Bo}{\omega \kappa \sin(\theta_s)} \frac{1}{\alpha Ca} \log \left( 1 + \frac{\alpha Ca \pi \omega}{\Delta} Z_0 \right). \quad (4.8)$$

In Fig. 8 we show the variation of  $t^*$  as a function of the key parameters of the problem. The time of arrest evidently increases with the initial interface deflection,  $Z_0$ , that sets the initial energy of the system, which must be dissipated to recover the rest configuration. A higher value of  $Z_0$  thus requires a longer time before the interface comes back to rest. However, dependence of  $t^*$  with respect to  $Z_0$  is logarithmic (see eq. (4.8)), such that the time of arrest increases less than linearly with  $Z_0$ . Regarding the slip coefficient  $\alpha$ , an increase of its value yields an increase of the damping rate, and, in turn, a decrease of  $t^*$ . This result remains true for all the values of  $\Delta$  considered (see Fig. 8b). The frequency  $\omega$  and the scalar quantity  $\kappa$  (introduced in eq. (3.33)) both arise from the first order problem. Consequently, they both depend on the static angle,  $\theta_s$ , and the

Bond number,  $Bo$ , in a complex way. As a consequence, no scaling law for  $t^*$  with  $\theta_s$  and  $Bo$  may be immediately deduced from equation (4.8) a priori. However, we have found numerically that both  $\omega$  and  $\kappa$  do not vary significantly with  $\theta_s$  and  $Bo$ , respectively. In Figure 8c the linear dependence of  $t^*$  with  $Bo$  is reported, whereas in Figure 8d we show that the time of arrest decreases when the static contact angle  $\theta_s$  is increased. This aspect is corroborated by the ratio  $Bo/\sin\theta_s$  in equation (4.8).

The dependence of  $t^*$  on  $Bo$  and  $\theta_s$  may be rationalized when recalling that the dissipation,  $\mathcal{D}$ , in a liquid wedge sliding on a solid substrate may be approximated in the following way (de Gennes *et al.* 2002):

$$\mathcal{D} \sim \sigma(\theta^2 - \theta_s^2) \sim \frac{1}{Bo}(\theta + \theta_s)(\theta - \theta_s). \quad (4.9)$$

The capillary-induced dissipation originates from the work of surface tension, which is non-zero only when the contact angle  $\theta$  deviates from its equilibrium value  $\theta_s$ . An increase in  $Bo$  lowers the dissipation and thus increases  $t^*$ . On the other hand, an increase in  $\theta_s$ , while keeping constant the contact line model parameters, is positively correlated with the dissipation: increasing  $\theta_s$ , while keeping constant  $\alpha$  and  $\Delta$ , merely translates upwards the plot in Figure 1b yielding the contribution  $\theta + \theta_s$  in equation (4.9) to increase while keeping constant  $\theta - \theta_s$ .

Finally, from the relative position of the curves displayed in Figure 8 obtained varying  $\Delta$ , we recover that an increase of  $\Delta$  always enhances the damping and lowers the value of  $t^*$ , consistently with equation (4.8).

#### 4.3. Comparison with the experiments of Cocciaro *et al.* (1993)

We now compare the weakly nonlinear analysis with the experimental observations of Cocciaro *et al.* (1993). Remarkably, these authors reports careful measurements of the contact line dynamics. In particular, they measure the contact line elevation,  $A_c$  according to their notation, and the dynamic contact angle,  $\theta$ , versus the tilt angle at the axis,  $\alpha_1$ . With this information and the assumption of sinusoidal motion of the contact line, which is supported by experimental evidence, it is possible to derive the contact angle as a function of the contact line velocity that is here reported in Figure 9(a). This behaviour well resembles the contact line law we have used in our analysis: a steep hysteresis range (of size  $\Delta = 43^\circ$ ) for small contact line velocity and a roughly linear dynamic range with  $\alpha_a \approx 100$  for advancing interface and  $\alpha_r \approx 200$  for the receding one. As previously discussed in the introduction (section 1), two different regimes are found by Cocciaro *et al.* (1993): at higher amplitude the contact line slides on the solid substrate and the fluid interface well matches the one of a free-edge mode. In contrast, at small amplitudes the pinned mode dominates the sloshing dynamics and the dynamic contact angle oscillates around its static value. The transition between the two regimes it is evident when the damping rate is monitored, see Figure 9(b) where the original data from Cocciaro *et al.* (1993) are reproduced (solid line) as a function of the contact line amplitude,  $A_c$ , rather than the amplitude of the tilt angle,  $\alpha_1$ , using their figure 3a for this conversion. When the wave amplitude is large ( $A_c > 2$  mm) the damping rate increases for a decreasing amplitude of oscillation until it reaches a maximum value. Then, in the transition between the two regimes the damping rate decreases until reaching a uniform value for the pinned motion, which is hardly visible in this representation (but clearly in their figure 9a).

As discussed above, our asymptotic analysis merely describes the dynamics of the free-edge mode that dominates the liquid sloshing in a circular container until the contact line starts to pin. A comparison with the experimental results of Cocciaro *et al.*

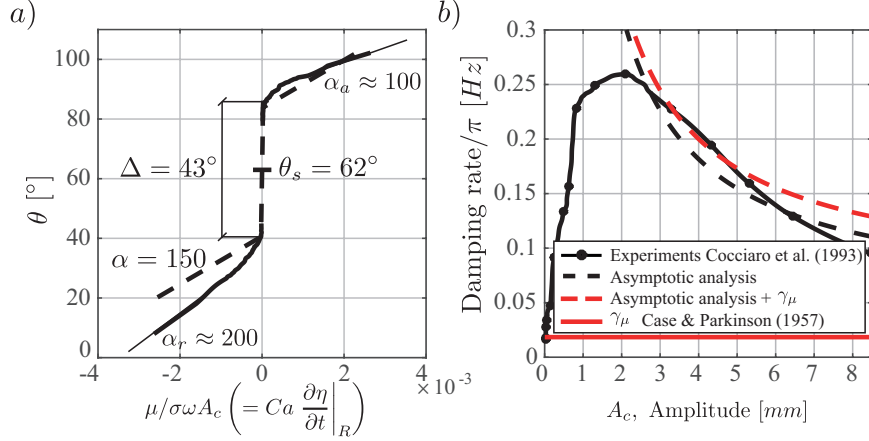


FIGURE 9. a) Contact line model corresponding to the experimental conditions of Cocciaro *et al.* (1993) as can be deduced from Figure 3 of their paper (solid line) and the contact line model used in this section (dashed line). b) Dimensional capillary induced damping rate over  $\pi$  versus the contact line amplitude as measured by Cocciaro *et al.* (1993) (solid line) at the container axis. The damping rate of the free-edge mode computed with the asymptotic analysis (dashed line) is computed using equation (4.5) and setting the physical parameters as in the experiment:  $\theta_s = 62^\circ$ ,  $Bo = 346.4$ ,  $Ca = 0.011$  and  $\Delta = 43^\circ$ ,  $\alpha = (\alpha_r + \alpha_a)/2 \approx 150$ . The damping rate due to the dissipation in the oscillating Stokes layer at the wall as found theoretically by Case & Parkinson (1957), see equation (4.10), is shown by the red line.

(1993) is then possible restricted to the case of higher amplitude ( $A_c > 2$  mm). With this aim, the damping rate computed with the asymptotic analysis are also shown in Figure 9(b) (dashed line). Due to the steep contact angle hysteresis observed in the contact law in Fig. 9(a), the damping rates are calculated by using equation (4.5) (Case II) and the other physical parameters are set as in the experiment:  $\Delta = 43^\circ$ ,  $\alpha = (\alpha_r + \alpha_a)/2 \approx 150$ ,  $\theta_s = 62^\circ$ ,  $Bo = 346.4$  and  $Ca = 0.011$ . Although the contact angle hysteresis,  $\Delta$ , and the slip coefficient,  $\alpha$ , are slightly larger with respect to the values allowed by the asymptotic machinery, the damping rates predicted by the asymptotic analysis well match, without any tunable parameter, the one measured experimentally by Cocciaro *et al.* (1993) in the high amplitude range ( $A_c > 2$  mm). Conversely, our theory does not capture the decreasing of the damping rate for lower amplitudes ( $A_c < 2$  mm).

We speculate that this discrepancy depends on the sticking of the interface at small amplitudes that requires the introduction of the pinned-edge mode to be described, which is not accounted for in our analysis. It has to be remarked, in fact, that the damping rate in the experiments was measured by measuring the tilt angle at the container's axis,  $\alpha_1$ , where both free-edge and pinned modes are present rather than at the contact line, where the pinned mode does not contribute. These two possible ways of measuring the wave decay are equivalent at large amplitudes but are different at small one (see Figure 3(a) of Cocciaro *et al.* (1993)). In particular, the damping rate measured at the contact line could have a diverging behaviour similar to what observed in our analysis since the contact line pins at a finite time and the free-edge mode expires.

In the same figure, we also show the viscous damping rate associated with the dissipation in the oscillating Stokes layers as found by the theory of Case & Parkinson (1957)

$$\gamma_\mu = \frac{3.52}{2\pi} \frac{\sqrt{\nu}}{R^{3/4}g^{1/4}}\omega. \quad (4.10)$$

The viscous damping rate,  $\gamma_\mu$  (red line), significantly underestimate the wave decay at higher amplitude and does not depend on the oscillation amplitude of the free surface, in disagreement with experimental results. At small amplitude,  $\gamma_\mu$ , is found close to the damping rate observed in the pinned regime, where the dissipation in the Stokes layer is not overshadowed anymore by the one in the dynamic meniscus.

## 5. Conclusions

We have presented a weakly nonlinear formulation for sloshing waves in a circular cylinder in partial wetting conditions. A nonlinear contact line model was incorporated in our asymptotic analysis as boundary condition at the moving contact line. In particular, we have adopted a contact line model where a steep dynamic hysteresis range is married to the widely used Hocking law, which is a linear relation. In the limit of steep dynamic hysteresis this model well mimics the experimental observations in unidirectional flows where both a static and dynamic hysteresis ranges are seen (Dussan 1979; Rio *et al.* 2005; Le Grand *et al.* 2005). In our asymptotic expansion, two distinguished solutions are considered depending on the steepness of the contact angle hysteresis that scales as  $\beta Ca \sim \epsilon^{-1}$  (case I) or as  $\beta Ca \sim \epsilon^{-2}$  (case II). In both cases, the zero order problem consists of the static meniscus shape in the cylindrical geometry considered. At first order, the linear problem satisfied by the sloshing gravity-capillary waves is obtained. The resulting global modes are neutrally stable since no dissipation source is found at zero and first order. Therefore, in the spirit of multiple scale analysis, a slowly varying amplitude and phase modulation are introduced at second order. They correspond to the weakly nonlinear correction accounting for capillary effects at the contact line.

The phase modulation is found not to enter at first order, so that capillary effects do not affect significantly the sloshing frequency. This result is in agreement with the experimental observations of Keulegan (1959) and Cocciaro *et al.* (1993) where a weak dependence on the amplitude has been observed for the oscillation frequency in partial wetting conditions.

Capillary effects however have a dramatic influence on the damping rate: the amplitude modulation results in a significant attenuation of the first order waves. According to the amplitude equations (3.34) and (3.44), capillary effects have two contributions to the damping rate: (i) a nonlinear contribution related to the contact angle hysteresis at small contact line velocities and (ii) a linear contribution imparted to the linear dependence between the contact angle and the contact line velocity. In our analysis, the capillary induced damping rate is found to depend on the wave amplitude. This fact is consistent with the experimental observations of Keulegan (1959); Cocciaro *et al.* (1993). The damping rate is first practically uniform when the wave amplitude is large, and then increases significantly at small amplitudes, as a consequence of the hysteresis contribution, although the details of the low amplitude behaviour depends on the scaling of the steepness parameter,  $\beta$ . In the case of steeper transitions between advancing and receding contact angle (case II,  $Ca\beta = \hat{\beta}/\epsilon^2$ ) the increase is such that the damping diverges in finite time leading to the arrest of the contact line motion.

We argue that this *finite time arrest* of the contact line could correspond to the transition from high to small amplitude observed experimentally by Cocciaro *et al.* (1993) when the free-edge mode expires and the bulk keeps a small amplitude motion following the pinned mode. The latter is not captured at order  $\epsilon$  but only in the non-resonant solution of the order  $\epsilon^2$  problem. One important limitation of our leading order model is therefore that it fails to capture the transition from free-end edge to pinned-end edge mode, because it only predicts the evolution of the amplitude  $A$  of the free-edge mode. This might

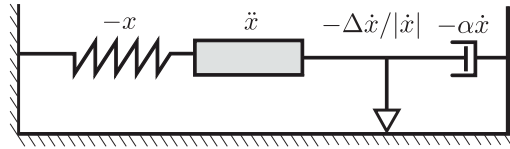


FIGURE 10. Schematic of the sloshing system with hysteresis: the inertial,  $\ddot{x}$ , and restoring,  $x$ , terms are balanced by linear,  $\alpha\dot{x}$ , and solid,  $\Delta\text{sgn}(\dot{x})$ , friction.

explain the discrepancy between the damping rate results reported in Figure 7(b), which account solely for the free-edge mode, and the ones in Figure 9 of Cocciaro *et al.* (1993) where the damping rate is measured at the container’s axis monitoring the superposition of the free-edge and pinned-edge modes. In any case we have shown that capillary effects modify the conventional physical picture associated with sloshing. In the previous case, these waves decay exponentially, thus virtually never exactly reach zero amplitude. With capillary effects this is no longer the case.

Experimental results leaning in the same direction have recently been reported in the case of biphasic systems, where capillary effects are emphasized using foam (Viola *et al.* 2016b). Adding foam to a liquid introduces nonlinear capillary forces which dramatically damp its oscillatory motion and lead the damping rate to increase at small oscillation amplitude. In the same work, the dynamics of sloshing with foam was modeled using a simple phenomenological oscillator derived by imposing the balance of the forces acting on the oscillating mass and using dimensional analysis. The same approach can be adopted here to derive a model equation for the single phase sloshing in the presence of steep dynamic hysteresis as in case II. We notice that the traction force pulling the meniscus toward the dry region, associated with the contact angle hysteresis, merely depends on the contact velocity through its sign. Specifically, this force is independent of the absolute value of the contact line velocity. As a result, this capillary-induced force may be interpreted as a Coulomb-like friction force, as already pointed out by Miles (1967) who derived an analytical expression for the damping rate of gravity waves subjected to a solid friction localized at the contact line. Conversely, the linear term in the contact line law (2.5) corresponds to a traction force, whose intensity is proportional to the contact line velocity in the limit of small contact angles. Combining these effects, we propose to model sloshing as an oscillator, subject to viscous damping – a traditional dissipation source – here augmented by an additional term analogous to solid friction. In Figure 10, we provide the sketch of a model system, mechanically equivalent to sloshing as described in our framework. It consists of a mass-spring element, a dashpot and a solid friction element:

$$\ddot{x} + x + \alpha\dot{x} + \Delta\dot{x}/|\dot{x}| = 0, \quad (5.1)$$

whose asymptotic solution reduces to the amplitude equation (3.44) in the limit of small coefficients  $\alpha$  and  $\Delta$ , further indication that the effect of the contact line hysteresis may be interpreted as Coulomb solid friction. An equation similar to (5.1) has been used by Noblin *et al.* (2004) to model the contact line dynamics of sessile drop subjected to vibrations, suggesting that our framework may be extended to other problems where the motion of a contact line is involved.

We finally note that the weakly nonlinear stability analysis carried out here provides a general framework to account for capillary effects in the surface gravity-capillary waves in a container. Indeed, contact line models other than the one used here can readily be introduced in the proposed formulation. Furthermore, accounting for the pinned-end edge mode, which dominates the bulk dynamics after the interface pinning, would be a

natural follow-up of the analysis introduced in this article.

The authors would like to acknowledge Giacomo Canevari and Antonio De Capua for fruitful discussions on functional analysis. Antonio Iubatti and Niccoló Discacciati are thanked for their help with preliminary numerical simulations. Financial support by ERC Grant No. SimCoMiCs 280117 is gratefully acknowledged.

## Appendix A. Numerical code

### A.1. Static meniscus

At order  $\epsilon^0$  the static meniscus shape in a cylindrical basin has to be determined. The governing equation (3.3) is discretized through Chebyshev collocation method and the Gauss-Lobatto-Chebyshev (GLC) collocation grid  $s \in [-1, 1]$  is mapped into the physical space  $r \in [0, R]$  through the linear mapping  $r = R(s + 1)/2$ . Hence the solution to the nonlinear equation is obtained by mean of an iterative Newton method which is made of the following steps:

- (a) Find an approximate guess solution  $\eta_0$  which satisfies the boundary conditions (3.4) and (3.5).
- (b) Solve for  $\delta\eta_0$  the linear system:

$$\left. \frac{d\chi(\eta)}{d\eta} \right|_{\eta_0} \delta\eta_0 = -\chi(\eta_0) \quad (\text{A } 1)$$

with homogeneous boundary conditions, where the Jacobian  $d\chi(\eta)/d\eta$  is defined in equation (3.9).

- (c) Set  $\eta_0 = \eta_0 + \delta\eta_0$
- (d) Compute the  $L_2$ -norm of  $\delta\eta_0$ . If  $\|\delta\eta_0\|_{L_2} > 10^{-12}$  go to step (b)
- (e) Set the static meniscus to  $\eta_0$

### A.2. Global stability analysis

At order  $\epsilon^1$  the linear eigenvalue problem (3.15) has to be solved and the equations together with the boundary conditions are discretized through Chebyshev collocation in a similar fashion to Viola *et al.* (2016a). The physical domain is in general not rectangular due to the presence of the static meniscus  $\eta_0$ . For this reason the physical domain with coordinates  $(r, z)$  has to be mapped into the Chebyshev space  $(s, t)$  through the transformation:

$$r = \frac{R}{2}(s + 1), \quad z = (t + 1) \left( \frac{H}{2} + \frac{\eta_0(s)}{2} \right) - H, \quad (\text{A } 2)$$

where  $\eta_0$  is the static meniscus. The partial derivatives in the physical space are related to the derivative in the computational space according to the relations:

$$\begin{aligned} \frac{\partial u}{\partial r} &= \frac{1}{r,s} u_{,s} - \frac{z_{,s}}{r,s z_{,t}} u_{,t} & \frac{\partial u}{\partial y} &= \frac{1}{z,t} u_{,t} \\ \frac{\partial^2 u}{\partial r^2} &= \frac{1}{r^2_{,s}} u_{,ss} + \frac{z^2_{,s}}{r^2_{,s} z^2_{,t}} u_{,tt} - \frac{z_{,t} z_{,ss} - 2z_{,s} z_{,st}}{r^2_{,s} z^2_{,t}} u_{,t} - \frac{2z_{,s}}{r^2_{,s} z_{,t}} u_{,st} & \frac{\partial^2 u}{\partial y^2} &= \frac{1}{z^2_{,t}} u_{,tt} \end{aligned} \quad (\text{A } 3)$$

where the derivatives of the physical coordinates with respect the computational coordinates depend on the mapping function, see Heinrichs (2004). In our case:

$$\begin{aligned} r_{,s} &= R & r_{,ss} &= 0 & r_{,t} &= 0 & r_{,st} &= 0 & r_{,tt} &= 0 \\ z_{,s} &= \frac{t+1}{2}\eta_{,s} & z_{,ss} &= \frac{t+1}{2}\eta_{,ss} & z_{,t} &= \frac{H}{2} + \frac{\eta(s)}{2} & z_{,st} &= \frac{\eta_{,s}}{2} & z_{,tt} &= 0 \end{aligned} \quad (\text{A } 4)$$

The integrals appearing in equations (3.33) are computed with Clenshaw-Curtis quadrature formula, where the quadrature weights are adapted to the mappings used following the method presented in Sommariva (2013). The number of nodes in the radial and vertical direction is  $N_r = N_z = 60$  which ensures convergence of the results. In Figure 8(d) the time of arrest as a function of  $\theta_s$  and  $\Delta$  computed with the finer grid  $N_r = N_z = 80$  is reported as proof of convergence.

## Appendix B. Adjoint equations

In this section we determine the adjoint equations to the first order problem (3.15), associated with the Hermitian scalar product:

$$\langle \mathbf{q}_\alpha, \mathbf{q}_\vartheta \rangle = \int_{\Omega} \overline{\Phi}_\alpha \Phi_\vartheta d\Omega + \int_{\eta_0} \overline{\eta}_\alpha \eta_\vartheta d\eta_0, \quad (\text{B } 1)$$

where the overline symbol designates the complex conjugate. The first term is a weighted volume integral with  $d\Omega = r dr dz$ . The second one corresponds to a surface integral on the zero-order surface  $\eta_0(r)$  with  $d\eta_0 = r dr \sqrt{1 + \eta_{0,r}^2}$ . In this section we will demonstrate that the first-order system of equations and boundary conditions are self-adjoint with respect to the scalar product (B 1).

By definition, the adjoint operator of the direct operator  $i\omega\mathcal{B} - \mathcal{A}$ , satisfies:

$$\langle \mathbf{q}^\dagger, (i\omega\mathcal{B} - \mathcal{A})\mathbf{q} \rangle = \langle (i\omega^\dagger\mathcal{B}^\dagger - \mathcal{A}^\dagger)\mathbf{q}^\dagger, \mathbf{q} \rangle. \quad (\text{B } 2)$$

where  $\mathbf{q}^\dagger = (\Phi^\dagger, \eta^\dagger)$  is a vector. Hence, the adjoint operator  $i\omega^\dagger\mathcal{B}^\dagger - \mathcal{A}^\dagger$  is derived by integration by parts, transferring the differential operators from the vector  $\mathbf{q}$  to the vector  $\mathbf{q}^\dagger$ . The boundary conditions for the adjoint operator are chosen so as to nullify the boundary integrals coming from the integration by parts. The rhs of equation (B 2) reads:

$$\int_{\Omega} \overline{\Phi}^\dagger \Delta \Phi d\Omega + \int_{\eta_0} \overline{\eta}^\dagger \left( i\omega\Phi + \eta - \frac{1}{Bo} \left[ \frac{a(r)}{r} \frac{\partial \eta}{\partial r} + b(r) \frac{\partial^2 \eta}{\partial r^2} - \frac{m^2 c(r)}{r^2} \eta \right] \right) \frac{d\eta_0}{\sqrt{1 + \eta_{0,r}^2}} = 0, \quad (\text{B } 3)$$

where we recall  $m$  is the azimuthal wavenumber, and integrating by parts we get:

$$\begin{aligned} & \int_{\Omega} \Delta \overline{\Phi}^\dagger \Phi d\Omega + \int_{\partial\Omega} \overline{\Phi}^\dagger \nabla \Phi \cdot \mathbf{n} dS - \int_{\partial\Omega} \Phi \nabla \overline{\Phi}^\dagger \cdot \mathbf{n} dS \\ & + \int_{\eta_0} -i\omega \overline{\eta}^\dagger \Phi r dr + \int_{\eta_0} \left( \overline{\eta}^\dagger - \frac{1}{Bo} \left[ \frac{a(r)}{r} \frac{\partial \overline{\eta}^\dagger}{\partial r} + b(r) \frac{\partial^2 \overline{\eta}^\dagger}{\partial r^2} - \frac{m^2 c(r)}{r^2} \overline{\eta}^\dagger \right] \right) \eta r dr \\ & - \frac{1}{Bo} \left[ r b(r) \left( \overline{\eta}^\dagger \frac{\partial \eta}{\partial r} - \frac{\partial \overline{\eta}^\dagger}{\partial r} \eta \right) \right]_{r=0}^{r=1} = 0. \end{aligned} \quad (\text{B } 4)$$

The first integral comes from the integration of continuity equation, and it is nullified by imposing the adjoint potential  $\Delta \Phi^\dagger = 0$  to be harmonic. The integrals on the domain

boundary  $\partial\Omega$  involving the normal velocity  $\nabla\Phi \cdot \mathbf{n}$  are the boundary terms resulting in the integration by parts of the continuity equation. These terms vanish at the solid wall because of the no-penetration condition,

$$\left. \frac{\partial\Phi}{\partial r} \right|_{r=1} = \left. \frac{\partial\Phi}{\partial z} \right|_{z=-h} = \left. \frac{\partial\Phi^\dagger}{\partial r} \right|_{r=1} = \left. \frac{\partial\Phi^\dagger}{\partial z} \right|_{z=-h} = 0, \quad (\text{B } 5)$$

and at the axis because of the symmetry condition:

$$\Phi|_{r=0} = \Phi^\dagger|_{r=0} = 0. \quad (\text{B } 6)$$

At the free interface the domain is curved, and the normal vector is  $\mathbf{n} = \frac{1}{\sqrt{(1+\eta_{0,r}^2)}} \begin{pmatrix} -\eta_{0,r} \\ 1 \end{pmatrix}$ . By using the kinematic boundary conditions (3.10) equation (B 4) reads:

$$\begin{aligned} & \int_{\eta_0} \left( -i\omega\bar{\eta}^\dagger + \eta_{0,r} \frac{\partial\bar{\Phi}^\dagger}{\partial r} - \frac{\partial\bar{\Phi}^\dagger}{\partial z} \right) \Phi \frac{d\eta_0}{\sqrt{1+\eta_{0,r}^2}} + \\ & + \int_{\eta_0} \left( -i\omega\bar{\Phi}^\dagger + \bar{\eta}^\dagger - \frac{1}{Bo} \left[ \frac{a(r)}{r} \frac{\partial\bar{\eta}^\dagger}{\partial r} + b(r) \frac{\partial^2\bar{\eta}^\dagger}{\partial r^2} - \frac{m^2 c(r)}{r^2} \bar{\eta}^\dagger \right] \right) \eta \frac{d\eta_0}{\sqrt{1+\eta_{0,r}^2}} \quad (\text{B } 7) \\ & - \frac{1}{Bo} \left[ r b(r) \left( \bar{\eta}^\dagger \frac{\partial\eta}{\partial r} - \frac{\partial\bar{\eta}^\dagger}{\partial r} \eta \right) \right]_{r=0}^{r=1} = 0. \end{aligned}$$

From the first two terms in equation (B 7) the adjoint kinematic and dynamic interface conditions are retrieved:

$$\begin{aligned} & -i\omega\bar{\eta}^\dagger + \eta_{0,r} \frac{\partial\bar{\Phi}^\dagger}{\partial r} - \frac{\partial\bar{\Phi}^\dagger}{\partial z} = 0 \\ & -i\omega\bar{\Phi}^\dagger + \bar{\eta}^\dagger - \frac{1}{Bo} \left[ \frac{a(r)}{r} \frac{\partial\bar{\eta}^\dagger}{\partial r} + b(r) \frac{\partial^2\bar{\eta}^\dagger}{\partial r^2} - \frac{m^2 c(r)}{r^2} \bar{\eta}^\dagger \right] = 0. \end{aligned} \quad (\text{B } 8)$$

To complete the adjoint system of equations the last term in equation (B 7), which comes from the integration by part of the capillary pressure in the direct dynamic condition, has to be nullified. In  $r = 0$  this term is null because of the integral argument is weighted by  $r$ . In contrast, at the contact line  $b(r = 1) = \sin^3(\theta_s)$  and the condition:

$$-\frac{\sin^3(\theta_s)}{Bo} \left( \bar{\eta}^\dagger \frac{\partial\eta}{\partial r} - \frac{\partial\bar{\eta}^\dagger}{\partial r} \eta \right) \Big|_{r=1} = 0 \quad (\text{B } 9)$$

defines the natural boundary condition at the contact line. In the case of free-end edge interface:

$$\left. \frac{\partial\eta}{\partial r} \right|_{r=1} = \left. \frac{\partial\bar{\eta}^\dagger}{\partial r} \right|_{r=1} = 0. \quad (\text{B } 10)$$

It should be noted that also the pinned boundary condition  $\eta = \bar{\eta}^\dagger = 0$  is a natural boundary condition of the problem. Hence the direct problem at order  $\epsilon$  is self-adjoint with respect to the Hermitian scalar product (B 1):

$$i\omega^\dagger \mathcal{B}^\dagger - \mathcal{A}^\dagger = -i\omega \mathcal{B} - \mathcal{A}, \quad (\text{B } 11)$$

with  $\omega^\dagger = -\omega$ . The vector  $\mathbf{q}^\dagger$  which satisfies the adjoint equations  $[-i\omega \mathcal{B} - \mathcal{A}]\mathbf{q}^\dagger = 0$  is the adjoint mode.

### Appendix C. Asymptotic analysis validation: comparison with direct numerical simulation

In this section the validity the weakly nonlinear analysis is discussed through a comparison with a direct numerical simulation of the governing equations presented in section 2, in the limit of small oscillations. The continuity equation

$$\Delta\Phi = 0, \quad (\text{C1})$$

is completed by the dynamic and kinematic conditions at the free-surface that in the case of static contact angle  $\theta_s = \pi/2$  read

$$\begin{aligned} \frac{\partial\Phi}{\partial t} + \eta - \frac{1}{Bo}\eta &= 0 \quad \text{at } z = 0, \\ \frac{\partial\eta}{\partial t} &= \frac{\partial\Phi}{\partial z}\Big|_0 \quad \text{at } z = 0. \end{aligned} \quad (\text{C2})$$

Symmetry conditions at the axis and no-penetration condition at the solid walls need also to be satisfied. The nonlinear wetting condition is then imposed at the contact line

$$-\frac{\partial\eta}{\partial r}\Big|_{r=1} = \alpha Ca \frac{\partial\eta}{\partial t}\Big|_{r=1} + \frac{\Delta}{2} \tanh\left(\beta Ca \frac{\partial\eta}{\partial t}\Big|_{r=1}\right) \quad \text{at } z = 0 \quad \text{and } r = 1. \quad (\text{C3})$$

In order to investigate the dynamics of the fundamental sloshing mode (first azimuthal mode) the state vector  $\mathbf{q}(t; r, \phi, z) = (\Phi, \eta)$  can be written as a truncated Fourier series,

$$\hat{\mathbf{q}}(t; r, \phi, z) = \hat{\mathbf{q}}_1(t; r, z)e^{i\phi} + c.c., \quad (\text{C4})$$

where *c.c.* stands for complex conjugate. By injecting the modal expansion (C4) in the nonlinear equation (C3) we get

$$-\frac{\partial\hat{\eta}_1}{\partial r}\Big|_{r=1} e^{i\phi} + c.c. = \alpha Ca \left( \frac{\partial\hat{\eta}_1}{\partial t}\Big|_{r=1} e^{i\phi} + c.c. \right) + \frac{\Delta}{2} \underbrace{\tanh\left(\beta Ca \left( \frac{\partial\hat{\eta}_1}{\partial t}\Big|_{r=1} e^{i\phi} + c.c. \right)\right)}_{\sum_n F_n e^{im\phi}}, \quad (\text{C5})$$

where the last term on the right-hand-side has to be Fourier transformed to get a boundary condition for the fundamental mode

$$\frac{\partial\hat{\eta}_1}{\partial r}\Big|_{r=1} e^{i\phi} + c.c. = -\alpha Ca \frac{\partial\hat{\eta}_1}{\partial t}\Big|_{r=1} e^{i\phi} - \frac{\Delta}{2} F_1(\beta, Ca, t)e^{i\phi} + c.c., \quad (\text{C6})$$

with

$$F_1(\beta, Ca, t) = \frac{1}{2\pi} \int_0^{2\pi} \tanh\left(\beta Ca \left( \frac{\partial\hat{\eta}_1}{\partial t}\Big|_{r=1} e^{i\phi} + c.c. \right)\right) e^{-i\phi} d\phi. \quad (\text{C7})$$

The resulting equations for  $\hat{\mathbf{q}}_1(t; r, z)$  are then discretized in space by means of a pseudospectral Chebyshev-Chebyshev method as introduced in section 3.2 and appendix A. A backward differentiation formula of second order is employed for time integration. This integration scheme is implicit and especially suited for solving stiff differential equations like our case where the continuity of mass (C1) is an algebraic constraint for the unsteady kinematic and boundary conditions (C2). The discretized state vector  $\mathbf{q}^n$  after  $n$  time steps of size  $\delta t$  is obtained by solving

$$\frac{3}{2}\mathcal{B}\mathbf{q}^n - 2\mathcal{B}\mathbf{q}^{n-1} + \frac{1}{2}\mathcal{B}\mathbf{q}^{n-2} = \delta t(\mathcal{A}\mathbf{q}^n + \mathbf{f}(v_c)) \quad (\text{C8})$$

where  $\mathcal{A}$  and  $\mathcal{B}$  contain the discretized equations, see equation (3.13). The vector  $\mathbf{f}(v_c)$  is null everywhere except for its component corresponding to the contact line ( $z = 0$  and  $r = 1$ ), which is equal to the last term of equation (C 6). The remaining term on the right-hand side of (C 6) is contained in  $\mathcal{B}$  while the left hand side of (C 6) is discretized in  $\mathcal{A}$ . The quantity  $v_c$  is the contact line velocity  $v_c = \frac{\partial \eta}{\partial t}|_{r=1}$  that can be treated explicitly or implicitly respectively. With an explicit scheme using the interface position at previous times,  $v_c$  reads

$$v_c = v_c^{n-1} = \frac{\eta_{n-1} + 4/3\eta_{n-2} + 1/3\eta_{n-3}}{2/3\delta t} \quad (\text{C 9})$$

and can be readily used to compute  $\mathbf{q}^n$ . In contrast, if an implicit formula is used, the velocity

$$v_c = v_c^n = \frac{\eta_n + 4/3\eta_{n-1} + 1/3\eta_{n-2}}{2/3\delta t}, \quad (\text{C 10})$$

depends on the unknown interface position  $\eta_n$  and an iterative procedure is needed due to the nonlinear relation  $\mathbf{f}(v_c)$ . In this case, in order to advance from the time  $t^{n-1}$  towards the next one  $t^n = t^{n-1} + \delta t$ , a guess contact line velocity  $v_c^{n*}$  is chosen (typically the one at previous time step  $v_c^{n-1}$ ) that is then used to compute  $\mathbf{q}^{n**}$  through equation (C 8). If the difference between the updated contact line velocity  $v_c^{n**}$  and the guess velocity is larger than a given threshold, the guess velocity is conveniently modified and the procedure repeated. This method has been implemented by using *fsolve*, a built-in Matlab function designed to solve nonlinear equations, which has been here employed to determine the contact line velocity  $v_c^n$  at every time-step. The two methods provide similar results. The implicit treatment of the contact line velocity allows for larger time step, typically  $\delta t = 0.05$  rather than  $\delta t = 0.01$  used in explicit case, but the subiterative procedure slows down computation speed.

Let us now compare the dynamics of the fundamental sloshing mode resulting from the numerical simulation with the one coming from the weakly nonlinear analysis introduced in the main body of the paper. In Figure 11 the contact line hysteresis is set to  $\Delta = 5^\circ$  whereas the steepness coefficient is varied as  $\beta = 100, 1000$  and  $10000$ , see Fig. 11 (a). The corresponding contact line motion is reported in Figure 11 (c,d,e) where the asymptotic solution (blue line) and its instantaneous amplitude (red line) well match the numerical results (circles) for all the values of  $\beta$ . Furthermore, a satisfactory agreement on the damping rate,  $\gamma(t)$ , is also observed, see Figure 11 (b). In particular, for  $\beta = 100$  the damping rate is practically uniform and increases almost linearly for  $\beta = 1000$ . In the case of higher steepness factor  $\beta = 10000$ ,  $\gamma(t)$  increases significantly, getting three times the initial value at  $t = 350$ .

In Figure 12 the steepness coefficient is fixed to  $\beta = 1000$  and the contact angle hysteresis is progressively increased as  $\Delta = 5^\circ, 10^\circ$  and  $20^\circ$ . The other parameters are set as in the previous case, see captions. The resulting contact line laws are shown in Figure 12 (a): the contact angle depends nonlinearly on the contact line velocity and the more  $\Delta$  increases, the more  $\theta$  varies. The resulting contact line motions as a function of time are shown in Figure 12(c,d,e) pointing to a good agreement between asymptotics and numerics. The damping rates are then shown in Figure 12 (e) thus revealing a stronger nonlinear behaviour for higher contact line hysteresis  $\Delta$  that is captured both from the asymptotic analysis and numerics.

Despite the good agreement between asymptotic analysis and numeric simulations, the steepness coefficient  $\beta$  and the hysteresis parameter  $\Delta$  could not be further increased in the numerical simulations with respect to the values reported here. This is due to the stiffness of the governing equations and the strong nonlinearity of the adopted contact

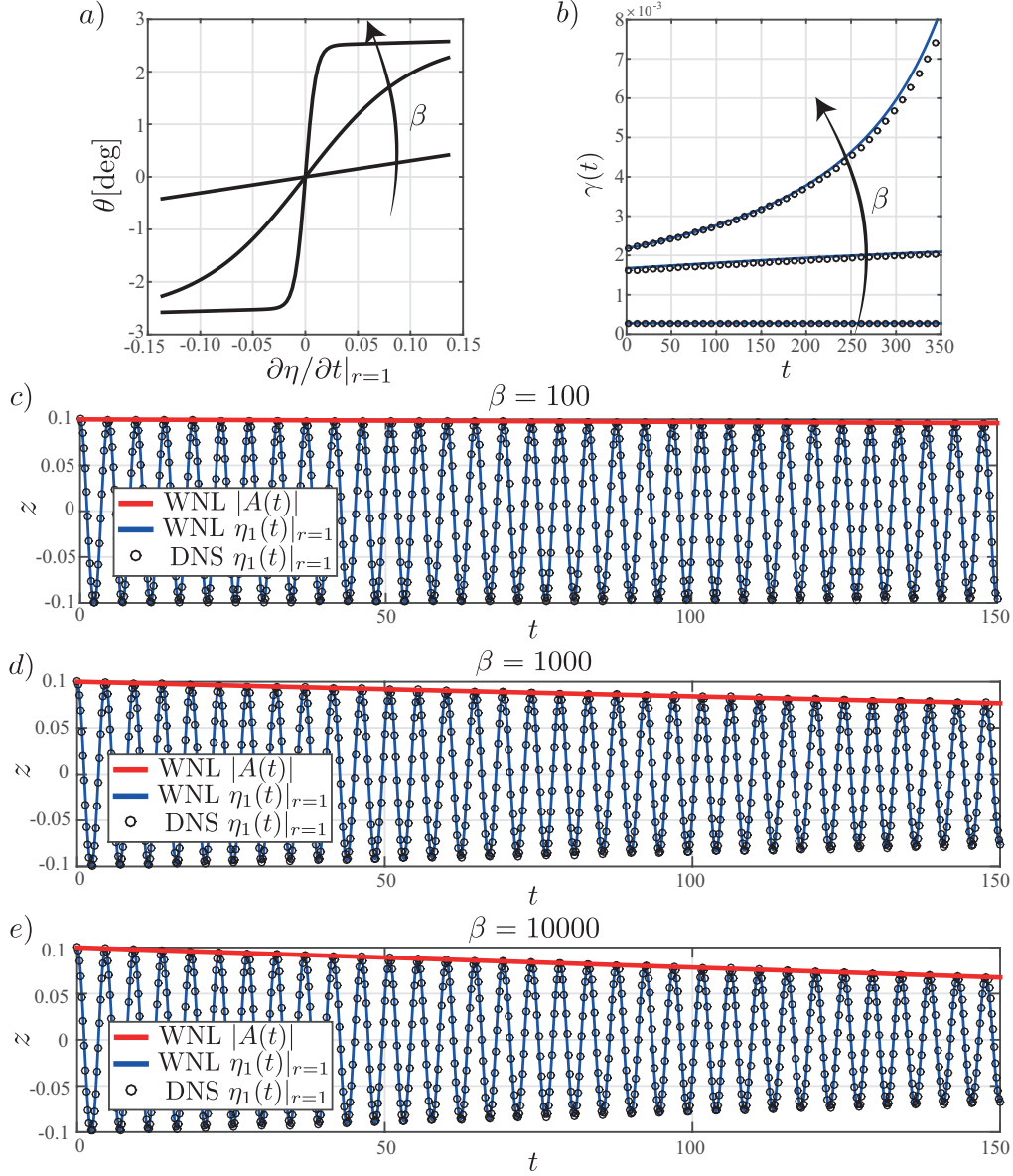


FIGURE 11. a) Contact line model for  $\Delta = 5^\circ$ ,  $\alpha = 1$ ,  $Bo = 500$ ,  $Ca = 0.01$  and  $\theta_s = \pi/2$ . The steepness coefficient is varied as  $\beta = 100$ , 1000 and 10000. The contact line motion according to the weakly nonlinear analysis (blue line, its amplitude is depicted by a red line) and the solution from numerics (circles) are shown for c)  $\beta = 100$ , d)  $\beta = 1000$  and e)  $\beta = 10000$ . The corresponding damping rates are reported in (b).

line law which arguably require more sophisticated time schemes to integrate the solution in the case of a steeper and more intense contact angle hysteresis.

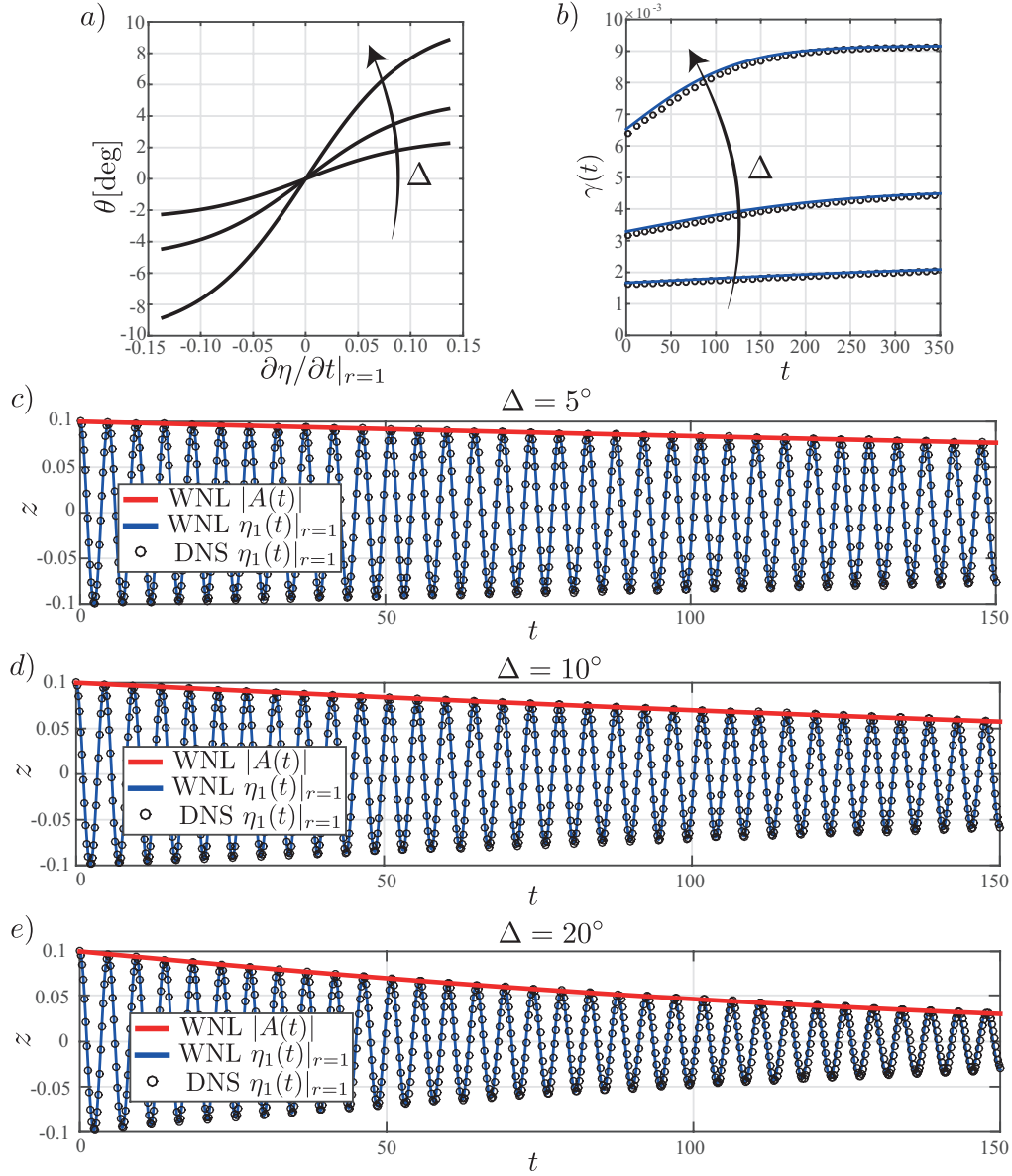


FIGURE 12. a) Contact line model for  $\beta = 1000$ ,  $\alpha = 1$ ,  $Bo = 500$ ,  $Ca = 0.01$  and  $\theta_s = \pi/2$ . The contact angle hysteresis is varied as  $\Delta = 5^\circ$ ,  $10^\circ$  and  $20^\circ$ . The contact line motion according to the weakly nonlinear analysis (blue line, its amplitude is depicted by a red line) and the solution from numerics (circles) are shown for c)  $\Delta = 5^\circ$ , d)  $\Delta = 10^\circ$  and e)  $\Delta = 20^\circ$ . The corresponding damping rates are reported in (b).

## REFERENCES

- BENJAMIN, T. B. & URSELL, F. 1954 The stability of the plane free surface of a liquid in vertical periodic motion. *Proceedings of the Royal Society of London. Series A, Mathematical and Physical Sciences* pp. 505–515.
- CASE, K.M. & PARKINSON, W.C. 1957 Damping of surface waves in an incompressible liquid. *Journal of Fluid Mechanics* **2** (02), 172–184.
- COCCIARO, B., FAETTI, S. & NOBILI, M. 1991 Capillarity effects on surface gravity waves in a cylindrical container: wetting boundary conditions. *Journal of Fluid Mechanics* **231**, 325–343.
- COCCIARO, B., FAETTI, S., NOBILI, M. & FESTA, C. 1993 Experimental investigation of capillarity effects on surface gravity waves: non-wetting boundary conditions. *Journal of Fluid Mechanics* **246**, 43–66.
- COX, R. G. 1986 The dynamics of the spreading of liquids on a solid surface. part 1. viscous flow. *Journal of Fluid Mechanics* **168**, 169–194.
- DE GENNES, P.-G. 1985 Wetting: statics and dynamics. *Reviews of modern physics* **57** (3), 827.
- DE GENNES, P.-G., BROCHARD-WYART, F., QUÉRÉ, D., FERMIGIER, M. & CLANET, C. 2002 *Gouttes, bulles, perles et ondes*. Belin Paris.
- DUSSAN, E.B. 1979 On the spreading of liquids on solid surfaces: static and dynamic contact lines. *Annual Review of Fluid Mechanics* **11** (1), 371–400.
- ERAL, H. B., 'T MANNETJE, J. C. M. & OH, J. M. 2013 Contact angle hysteresis: a review of fundamentals and applications. *Colloid and polymer science* **291** (2), 247–260.
- HEINRICH, W. 2004 Spectral collocation schemes on the unit disc. *Journal of Computational Physics* **199** (1), 66–86.
- HOCKING, L.M. 1987 The damping of capillary-gravity waves at a rigid boundary. *Journal of Fluid Mechanics* **179**, 253–266.
- JIANG, L., PERLIN, M. & SCHULTZ, W.W. 2004 Contact-line dynamics and damping for oscillating free surface flows. *Physics of Fluids (1994-present)* **16** (3), 748–758.
- KEULEGAN, G.H. 1959 Energy dissipation in standing waves in rectangular basins. *Journal of Fluid Mechanics* **6** (01), 33–50.
- LAMB, H. 1932 *Hydrodynamics*. Cambridge university press.
- LE GRAND, N., DAERR, A. & LIMAT, L. 2005 Shape and motion of drops sliding down an inclined plane. *Journal of Fluid Mechanics* **541**, 293–315.
- LEGER, L. & JOANNY, J.F. 1992 Liquid spreading. *Reports on Progress in Physics* **55** (4), 431.
- MILES, J.W. 1967 Surface-wave damping in closed basins. In *Proceedings of the Royal Society of London A: Mathematical, Physical and Engineering Sciences*, , vol. 297, pp. 459–475. The Royal Society.
- NAYFEH, A.H. 2008 *Perturbation methods*. John Wiley & Sons.
- NOBLIN, X., BUGUIN, A. & BROCHARD-WYART, F. 2004 Vibrated sessile drops: Transition between pinned and mobile contact line oscillations. *The European Physical Journal E: Soft Matter and Biological Physics* **14** (4), 395–404.
- PUTHENVEETIL, B.A., SENTHILKUMAR, V.K. & E.J.HOPFINGER 2013 Motion of drops on inclined surfaces in the inertial regime. *Journal of Fluid Mechanics* **726**, 26–61.
- RIO, E., DAERR, A., ANDREOTTI, B. & LIMAT, L. 2005 Boundary conditions in the vicinity of a dynamic contact line: experimental investigation of viscous drops sliding down an inclined plane. *Physical review letters* **94** (2), 024503.
- SOMMARIVA, A. 2013 Fast construction of Fejér and ClenshawCurtis rules for general weight functions. *Computers & Mathematics with Applications* **65** (4), 682–693.
- STUART, J.T. 1960 On the non-linear mechanics of wave disturbances in stable and unstable parallel flows part 1. the basic behaviour in plane poiseuille flow. *Journal of Fluid Mechanics* **9** (03), 353–370.
- URSELL, F. 1952 Edge waves on a sloping beach. In *Proceedings of the Royal Society of London A: Mathematical, Physical and Engineering Sciences*, , vol. 214, pp. 79–97. The Royal Society.
- VIOLA, F., ARRATIA, C. & GALLAIRE, F. 2016a Mode selection in trailing vortices: harmonic response of the non-parallel batchelor vortex. *Journal of Fluid Mechanics* **790**, 523–552.

- VIOLA, F., BRUN, P.-T., DOLLET, B. & GALLAIRE, F. 2016*b* Foam on troubled water: Capillary induced finite-time arrest of sloshing waves. *Physics of Fluids (1994-present)* **28** (9), 091701.
- VOINOV, O. V. 1976 Hydrodynamics of wetting. *Fluid Dynamics* **11** (5), 714–721.